

Helical Topological Superconducting Pairing at Finite Excitation Energies

Masoud Bahari,^{1,2,*} Song-Bo Zhang,^{3,4} Chang-An Li,^{1,2} Sang-Jun Choi,⁵ Philipp Rößmann,^{1,2,6} Carsten Timm,^{2,7} and Björn Trauzettel^{1,2}

¹*Institute for Theoretical Physics and Astrophysics, University of Würzburg, D-97074 Würzburg, Germany*

²*Würzburg-Dresden Cluster of Excellence ct.qmat, Germany*

³*Hefei National Laboratory, Hefei, Anhui, 230088, China*

⁴*International Center for Quantum Design of Functional Materials (ICQD), University of Science and Technology of China, Hefei, Anhui, 230026, China*

⁵*Department of Physics Education, Kongju National University, Gongju 32588, Republic of Korea*

⁶*Peter Grünberg Institut, Forschungszentrum Jülich and JARA, D-52425 Jülich, Germany*

⁷*Institute of Theoretical Physics, Technische Universität Dresden, 01062 Dresden, Germany*

(Dated: April 22, 2024)

We propose helical topological superconductivity away from the Fermi surface in three-dimensional time-reversal-symmetric odd-parity multiband superconductors. In these systems, pairing between electrons originating from different bands is responsible for the corresponding topological phase transition. Consequently, a pair of helical topological Dirac surface states emerges at finite excitation energies. These helical Dirac surface states are tunable in energy by chemical potential and strength of band-splitting. They are protected by time-reversal symmetry combined with crystalline two-fold rotation symmetry. We suggest concrete materials in which this phenomenon could be observed.

Introduction.—The search for intrinsic topological superconductors has been an active research area in the condensed matter community for many years [1–5]. In weakly interacting systems, the essential ingredient for intrinsic topological phase transitions (TPTs) is a weak attractive electron-electron interaction appearing close to the Fermi surface. This results in particular bulk properties including topological superconducting gaps [6–18], possibly with nodes [19–28]. Due to particle-hole symmetry, the bulk-boundary correspondence allows for emergent Majorana boundary states protected by band topology.

Finite energy (FE) Cooper pairing is a particular type of pairing that can happen away from the Fermi surface [29–37]. It arises from multiband effects in superconductors [38–55]. Dips in the density of states at FEs is a particular spectral feature of such pairing found in hybrid structures based on the superconducting proximity effect of NbSe₂ in the topological insulators BiSbTe_{1.25}Se_{1.75} [56] and Bi₂Se₃ [57]. In this Letter, we show that TPTs can be exclusively induced by FE Cooper pairing emerging from time-reversal-symmetric odd-parity multiband superconductors. The interplay of spin-orbit coupling and electron-phonon interaction allows for the formation of unconventional FE Cooper pairing with topologically nontrivial order. Bulk band crossings are partially gapped out in momentum space at FEs due to odd-parity superconductivity. This leads to TPTs as evidenced by helical topological Dirac surface states at finite excitation energies. Such surface states are composed of electrons and holes with different magnetic quantum numbers. They are distinct from conventional Majorana boundary states due to broken particle-hole symmetry away from the Fermi energy. The helical Dirac points are (i) protected topologically by time-reversal \hat{T} symmetry

combined with crystalline two-fold rotation as we specify below, and (ii) tunable in energy by chemical potential and strength of band splitting.

To observe FE Cooper pairing, the normal state should have at least two energy bands with the same sign of curvature close to the Fermi energy. The bands need to have different effective masses. Therefore, our results are relevant for a broad range of multiband superconductors as we elaborate on below.

To capture the underlying physics, we develop a theory for generic superconducting multiband systems with four-valued local degrees of freedom. For concreteness, we work with a model Hamiltonian describing the band structure of electrons with effective angular momentum $j = 3/2$ near the Fermi energy. However, the formalism is not restricted to this particular choice of angular momentum quantum numbers.

Model.—We start with the Luttinger-Kohn Hamiltonian $\hat{\mathcal{H}}_{\mathbf{k}} = \alpha|\mathbf{k}|^2 + \beta(\mathbf{k} \cdot \mathbf{J})^2 - \mu$, which describes $j = 3/2$ electrons within the Γ_8 bands [24, 58–60]. The kinetic, symmetric spin-orbit-coupling, and chemical potential terms are parameterized by α , β , and μ , respectively. $\mathbf{k} = (k_x, k_y, k_z)$ is the three-dimensional (3D) momentum and $\mathbf{J} = (\hat{J}_x, \hat{J}_y, \hat{J}_z)$ are the 4×4 spin matrices in the $j = 3/2$ formalism. The normal state has a pair of doubly degenerate quadratic energy bands given by $E_{\mathbf{k}}^+ = (\alpha + 9\beta/4)|\mathbf{k}|^2 - \mu$ and $E_{\mathbf{k}}^- = (\alpha + \beta/4)|\mathbf{k}|^2 - \mu$. The chemical potential μ should fulfill $|\mu| < N\hbar\omega_D$, where ω_D is the Debye frequency and $N = 1.25 + \alpha/\beta$ is a material dependent number. While $\hat{\mathcal{H}}_{\mathbf{k}}$ preserves $O(3)$ symmetry, our predictions are generic and can be applied to systems with relevant point group symmetry in the normal state [61].

The superconducting properties of the system can be captured by the Bogoliubov-de Gennes (BdG) Hamilto-

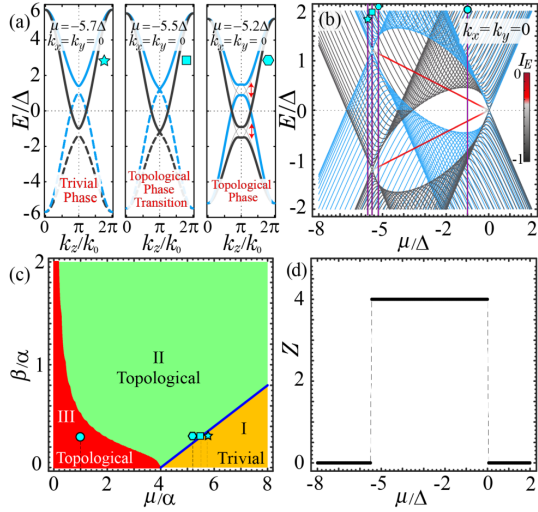


Figure 1. (a) BdG energy spectra along the [001] direction for three different values of the chemical potential. Solid (dashed) lines depict twofold degenerate particle (hole) bands. Decoupled energy bands are plotted with distinct colors (blue and black) due to \hat{C}_P symmetry. In the third panel, the fade gray lines denote $\Delta = 0$. (b) Spectrum versus μ for a (001) slab with 80 layers. The color bar indicates the inverse participation ratio [69]. The gray and blue colors represent bulk states, and red color denotes edge states. (c) Topological phase diagram induced by FE pairing. Region III (II) indicates that the helical Dirac points are located (coexist) within the low energy gap (bulk states). (d) Topological invariant corresponding to panel (b). A_{2u} pairing is responsible for superconductivity in all panels. Other parameters are $\beta = 0.3\alpha$, $\alpha = -\Delta$ and $k_0 = a^{-1}$ with a being the lattice constant in corresponding tight-binding calculations.

nian

$$\hat{H}(\mathbf{k}) = \begin{pmatrix} \hat{\mathcal{H}}_{\mathbf{k}} & \hat{\Delta}_{\mathbf{k}} \\ \hat{\Delta}_{\mathbf{k}}^\dagger & -\hat{\mathcal{H}}_{-\mathbf{k}}^T \end{pmatrix}, \quad (1)$$

where $\hat{\mathcal{H}}_{\mathbf{k}}$ is the inversion-symmetric normal part and $\hat{\Delta}_{\mathbf{k}}$ is a 4×4 pairing matrix describing pairing of electrons with four-valued degrees of freedom. Generally, the explicit form of $\hat{\Delta}_{\mathbf{k}}$ depends on the basis of the system. For concreteness, we focus on systems with cubic point group O_h . In this case, $\hat{\Delta}_{\mathbf{k}}$ can be expanded into irreducible tensor operators of irreducible representations (irreps) of O_h [34, 62–64].

Topology at finite energies.—The prerequisite for TPTs away from the Fermi energy is that the $E_{\mathbf{k}}^+$ electron and $-E_{\mathbf{k}}^-$ hole bands cross each other. These band crossings become anti-crossings in the presence of odd-parity FE Cooper pairing as we explain in detail in the Supplemental Material (SM) [65]. For concreteness, we consider the A_{2u} (p -wave septet) pairing given by $\hat{\Delta}_{\mathbf{k}} = \Delta(\mathbf{k} \cdot \hat{\mathbf{T}})\hat{\mathcal{R}}$, where Δ is the pairing strength, $\hat{\mathcal{R}} = e^{i\pi\hat{J}_y}$ is the fermionic antisymmetry factor, and $\hat{T}_i = \{\hat{J}_i, \hat{J}_{i+1}^2 - \hat{J}_{i+2}^2\}$ with $i+1 = y$ if $i = x$, etc., cyclically [60, 62]. Note that

O_h		\mathbf{k}	$\hat{\Delta}_{\mathbf{k}}^{+-} = \Delta \times$
E_u	$E_u^{(2)}$	$(0, 0, k_z)$	$k_z \hat{\tau}_0$
T_{2u}	$T_{2u}^{(1)}$	$(0, 0, k_z)$	$k_z \hat{\tau}_z$
	$T_{2u}^{(2)}$	$(0, k_y, 0)$	$k_y \hat{\tau}_x$
	$T_{2u}^{(3)}$	$(k_x, 0, 0)$	$ik_x \hat{\tau}_x$
A_{2u}		$(k_x, 0, 0)$	$-k_x \hat{\tau}_0$
		$(0, k_y, 0)$	$-ik_y \hat{\tau}_z$
T_{2u}	$T_{2u}^{(1)}$	$(0, 0, k_z)$	$k_z \hat{\tau}_0$
		$(0, 0, k_z)$	$k_z \hat{\tau}_z$
		$(\pm k, \pm k, 0)$	$k(\pm \hat{\tau}_0 \pm i \hat{\tau}_z)$
	$T_{2u}^{(2)}$	$(k_x, 0, 0)$	$k_x \hat{\tau}_x$
		$(0, \pm k, \pm k)$	$k(\hat{\tau}_y \pm \hat{\tau}_z/3)$
	$T_{2u}^{(3)}$	$(0, k_y, 0)$	$k_y \hat{\tau}_x$
		$(\pm k, 0, \pm k)$	$k(\pm \hat{\tau}_0/3 - i \hat{\tau}_y)$

Table I. TPTs at FEs in p -wave pairing channels distinguished by cubic irreps (first column) and their components (second column). The direction of TPTs is denoted in the third column. The last column indicates the FE pairing potential responsible for TPTs. The pairing matrices for the given irreps are given in the SM [65, 71].

p -wave septet pairing has been argued to be the favorable pairing symmetry in systems with cubic symmetry [60, 66, 67]. Although we focus on this specific pairing channel, our qualitative results are general. They apply to several odd-parity pairing channels summarized in Table I.

Without loss of generality, we illustrate our predictions for the [001] direction (i.e., $k_x = k_y = 0$). We observe in Fig. 1(a) that the bulk bands, i.e., electron $E_{k_z}^+$ and hole $-E_{k_z}^-$ branches, do not touch each other for $\mu = -5.7\Delta$ close to $k_z = \pi$ away from the Fermi surface. In this case, the system exhibits a topologically trivial phase. Increasing slightly the Fermi energy to $\mu = -5.5\Delta$, this makes the two bands touch each other. For $\mu = -5.2\Delta$, the presence of FE pairing, i.e., pairing between electrons with different magnetic quantum numbers ($|m_j| = 3/2$ with $|m_j| = 1/2$), opens a band gap indicating a TPT. This TPT is accompanied by the emergence of helical topological surface states. To illustrate the appearance of helical surface states (HSSs), the spectrum of a finite system is depicted in Fig. 1(b) [68]. The localized fourfold degenerate HSSs are marked by red color indicating large inverse participation ratio (IPR) [69]. They emerge within the range of Fermi energies $\mu/\Delta \in [-5.5, 0]$, in which a nonzero topological invariant, see Fig. 1(d), can be found. We describe below how the topological invariant is defined. Generally, when the energy bands have downward (upward) curvature, i.e., $\text{sgn}(\alpha) = \text{sgn}(\beta) = -(+)$, the topological phase occurs in the range $\mu/\Delta \in [\mu_c, 0]$ ($[0, \mu_c]$) with the critical value $\mu_c = 4\alpha + 5\beta$. The analysis of the spectrum along other directions reveals that these HSSs are helical topological Dirac points occurring at finite exci-

tation energies as shown in Fig. 2. Notably, the helical surface points do not hybridize with the bulk states due to the combination of time-reversal and two-fold rotation symmetries [70].

According to the topological phase diagram, depicted in the plane of $(\mu/\alpha, \beta/\alpha)$ in Fig. 1(c), the FE Cooper pairing in odd-parity multiband superconductors is intrinsically topological (regions II and III) within a certain range of Fermi energies.

Theory for topological phase transition.—The nontrivial topology at FEs originates from unconventional pairing of FE electrons. To understand the underlying mechanism, we project the BdG Hamiltonian onto the doubly degenerate eigenspinors of the normal state $\hat{V}_{\mathbf{k}}^{\pm}$ as the pseudospin basis. In this basis, the inter-band representation of the BdG Hamiltonian becomes

$$\hat{\mathcal{H}}(\mathbf{k}) = \begin{pmatrix} \hat{H}_{\mathbf{k}}^{+-} & \hat{\Delta}_{\mathbf{k}}^{\text{intra}} \\ (\hat{\Delta}_{\mathbf{k}}^{\text{intra}})^{\dagger} & \hat{H}_{\mathbf{k}}^{-+} \end{pmatrix}, \quad (2)$$

where $\hat{H}_{\mathbf{k}}^{+-}$ and $\hat{H}_{\mathbf{k}}^{-+}$ denote the interband parts of the BdG Hamiltonian and $\hat{\Delta}_{\mathbf{k}}^{\text{intra}}$ describes intraband pairing at the Fermi energy. The subblock matrices in Eq. (2) can be written as

$$\hat{H}_{\mathbf{k}}^{+-} = \begin{pmatrix} E_{\mathbf{k}}^{+} & \hat{\Delta}_{\mathbf{k}}^{+-} \\ (\hat{\Delta}_{\mathbf{k}}^{+-})^{\dagger} & -E_{\mathbf{k}}^{-} \end{pmatrix}, \quad \hat{\Delta}_{\mathbf{k}}^{\text{intra}} = \begin{pmatrix} 0 & \hat{\Delta}_{\mathbf{k}}^{++} \\ (\hat{\Delta}_{\mathbf{k}}^{--})^{\dagger} & 0 \end{pmatrix}, \quad (3)$$

where $\hat{\Delta}_{\mathbf{k}}^{\nu\nu'}$ with $\nu, \nu' \in \{+, -\}$ denotes the pairing potential projected onto the normal state bands defined by $\hat{\Delta}_{\mathbf{k}}^{\nu\nu'} = \hat{V}_{\mathbf{k}}^{\nu\dagger} \hat{\Delta}_{\mathbf{k}} (\hat{V}_{-\mathbf{k}}^{\nu'})^T$ where $\nu \neq \nu'$ ($\nu = \nu'$) indicates inter- (intra-) band pairing between electrons having different (identical) magnetic quantum numbers in magnitude. In our model, the most convenient way to explain TPTs at FEs is to make $\hat{\mathcal{H}}(\mathbf{k})$ block diagonal. Thus, TPTs occur in directions in momentum space where the odd-parity interband pairing is finite, whereas the intraband pairing vanishes (nodes at the Fermi energy), i.e., $\hat{\Delta}_{\mathbf{k}}^{\nu\nu'} \neq 0$ and $\hat{\Delta}_{\mathbf{k}}^{\text{intra}} = 0$. These conditions are satisfied, particularly for the A_{2u} pairing, when time-reversal symmetry combines with a two-fold rotation around the $\langle 110 \rangle$ direction. This combination is expressed as $\hat{C}_T = \hat{T} \hat{C}_{2,x+y}$ yielding $\hat{C}_T^2 = 1$ [63, 65, 72–78]. Consequently, the point nodes emerge at the Fermi energy accompanied by nonvanishing interband pairing along the $\langle 001 \rangle$ direction. In this case, Eq. (2) becomes block diagonal and $\hat{H}_{\mathbf{k}}^{\nu\nu'}$ is further reducible. To block diagonalize $\hat{H}_{\mathbf{k}}^{\nu\nu'}$, we define a general rotation symmetry operator in interband basis

$$\hat{D}_{\mathbf{n}}(\theta, \epsilon) \equiv \text{diag}(e^{i\theta/2(\mathbf{n}\cdot\hat{\tau})}, \epsilon e^{-i\theta/2(\mathbf{n}\cdot\hat{\tau})}), \quad (4)$$

where θ is the rotation angle about an arbitrary unit vector \mathbf{n} . The vector of Pauli matrices in pseudospin basis is $\hat{\tau} = (\hat{\tau}_x, \hat{\tau}_y, \hat{\tau}_z)$ and $\epsilon = \pm 1$ stands for two unitarily equivalent representations. Along the TPT directions,

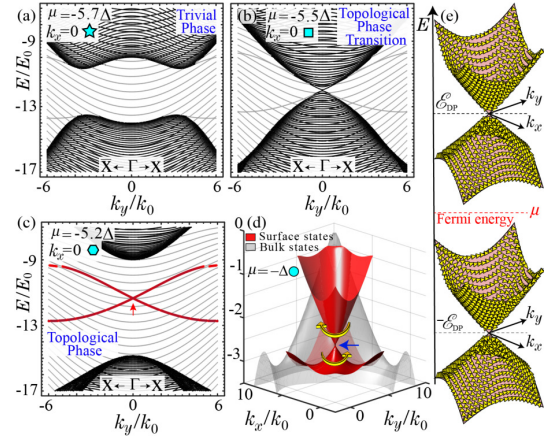


Figure 2. Spectra of a slab with (001) surfaces as a functions of k_y indicating (a) topologically trivial phase, (b) topological phase transition, and (c) topological phase at FEs. The thickness is 200 layers. (d) 3D energy dispersion versus k_x and k_y . (e) Helical surface cones at positive and negative energies related by particle-hole symmetry. (d,e) Yellow arrows indicate left- (right-) handed spin texture in the upper (lower) cone. $E_0 = 0.1\Delta$ and other parameters are the same as in Fig. 1.

the superconducting Hamiltonian of each block preserves a two-fold rotation by $\theta = \pi$, i.e., $[\hat{D}_{\mathbf{n}}(\pi, \epsilon), \hat{H}_{\mathbf{k}}^{\nu\nu'}] = 0$. This allows us to label the corresponding energy bands by the sign \pm corresponding to the eigenvalues $\lambda = \pm i$ of $\hat{D}_{\mathbf{n}}(\pi, \epsilon)$. This operation satisfies the property $\hat{D}_{\mathbf{n}}^2(\pi, \epsilon) = -\hat{1}$ [79]. $\hat{H}_{\mathbf{k}}^{\nu\nu'}$ can be reduced to two independent subblock matrices in the eigenspaces of $\hat{D}_{\mathbf{n}}(\pi, \epsilon)$. The corresponding similarity transformation is $\hat{U}^{\dagger} \hat{H}_{\mathbf{k}}^{\nu\nu'} \hat{U} = \text{diag}(\hat{h}_{\mathbf{k},-}^{\nu\nu'}, \hat{h}_{\mathbf{k},+}^{\nu\nu'})$, where \hat{U} is the unitary matrix defined by the eigenvectors of $\hat{D}_{\mathbf{n}}(\pi, \epsilon)$. Then, $\hat{h}_{\mathbf{k},\lambda}^{\nu\nu'}$ becomes

$$\hat{h}_{\mathbf{k},\lambda}^{\nu\nu'} = \begin{pmatrix} -E_{\mathbf{k}}^{\nu'} & (\delta_{\mathbf{k},\lambda}^{\nu\nu'})^* \\ \delta_{\mathbf{k},\lambda}^{\nu\nu'} & E_{\mathbf{k}}^{\nu} \end{pmatrix}, \quad (5)$$

where $\delta_{\mathbf{k},\lambda}^{\nu\nu'}$ is the FE pairing represented in the eigenbasis of $\hat{D}_{\mathbf{n}}(\pi, \epsilon)$ [80]. Eventually, the transformed BdG Hamiltonian, Eq. (2), decouples into four 2×2 subblocks,

$$\hat{\mathcal{H}}'(\mathbf{k}) = \text{diag}(\hat{h}_{\mathbf{k},+}^{+-}, \hat{h}_{\mathbf{k},-}^{+-}, \hat{h}_{\mathbf{k},+}^{-+}, \hat{h}_{\mathbf{k},-}^{-+}). \quad (6)$$

Note that $\hat{\mathcal{H}}'(\mathbf{k})$ illustrates the decoupling of the double degeneracy of states. For the A_{2u} pairing channel, this is achieved through the mirror reflection symmetry $\hat{C}_P = \hat{P} \hat{C}_{2,x+y}$, where \hat{P} is inversion symmetry, yielding $\hat{C}_P^2 = -1$ (see Fig. 1(a)).

The topological properties at FEs are encoded in the subblocks of $\hat{\mathcal{H}}'(\mathbf{k})$. Generically, when the pairing term in $\hat{h}_{\mathbf{k},\lambda}^{\nu\nu'}$ is odd in momentum, the FE bulk band gaps between electron and hole branches cross or anticross at the parity-invariant momenta. This happens through the tuning of the normal state parameters, i.e., (α, β, μ) , and

leads to a topologically nontrivial phase as described below.

The topological classification of our 3D model in class DIII is captured by a \mathbb{Z} topological index at low energies [81–86]. We are, however, interested in a different type of topological classification at finite excitation energies. This classification is based on the sum of four \mathbb{Z}_2 indices stemming from a quantization of the Berry phase defined for each block presented in Eq. (6). Note that $\hat{h}_{\mathbf{k},-}^{+-}$ is essentially a replica of $\hat{h}_{\mathbf{k},+}^{+-}$, owing to the presence of $\hat{\mathcal{D}}_{\mathbf{n}}(\pi, \epsilon)$ symmetry. Additionally, $\hat{h}_{\mathbf{k},\pm}^{-+}$ represent the particle-hole counterparts of $\hat{h}_{\mathbf{k},\pm}^{+-}$. Therefore, the decoupled sectors in Eq. (6) are topologically identical. The topological invariant is given by $Z = \sum_{\lambda\nu\nu'} N_{\lambda}^{\nu\nu'}$ with \mathbb{Z}_2 index $N_{\lambda}^{\nu\nu'} = (1/\pi) \oint_c d\mathbf{k} \cdot i \langle u_{\mathbf{k},\lambda}^{\nu\nu'} | \nabla_{\mathbf{k}} | u_{\mathbf{k},\lambda}^{\nu\nu'} \rangle$, where $|u_{\mathbf{k},\lambda}^{\nu\nu'}\rangle$ is the eigenspinor of $\hat{h}_{\mathbf{k},\lambda}^{\nu\nu'}$ associated with the lower energy band [87–90]. In the topological phase, $N_{\lambda}^{\nu\nu'}$ is quantized due to parity symmetry implied by $\hat{\tau}_z \hat{h}_{\mathbf{k},\lambda}^{\nu\nu'} \hat{\tau}_z^{-1} = \hat{h}_{-\mathbf{k},\lambda}^{\nu\nu'}$. We obtain analytically that $\hat{h}_{\mathbf{k},\lambda}^{\nu\nu'}$ is topologically nontrivial with $N_{\lambda}^{\nu\nu'} = 1$, when $\mu/\Delta \in [\mu_c, 0]$ ($[0, \mu_c]$) for $\text{sgn}(\alpha) = \text{sgn}(\beta) = -(+)$. The topological phase diagram in Fig. 1(c) illustrates this analysis [91]. The topological index becomes a net value of $Z = 4$ indicating the emergence of two pairs of helical Dirac states on the surface of superconductor, cf. Fig. 2(e). One helical pair appears at positive excitation energy while the other pair emerges at negative excitation energy [92].

2D surface states.— The HSSs disperse linearly in the vicinity of the Γ point of the 2D surface Brillouin zone as illustrated in Fig. 2(c) and 2(d). At larger momenta, the surface dispersion connects to the bulk states. This is due to the intraband pairing at the Fermi energy, i.e., $\hat{\Delta}_{\mathbf{k}}^{\text{intra}}$. It is finite for nonvanishing k_x or k_y . Hence, $\hat{\mathcal{H}}'(\mathbf{k})$ is no longer block-diagonal. This lifts the twofold degeneracy except at the Dirac points, which is the reason for the emergence of helical Dirac surface cones at FEs.

To gain insight into the dispersion of the HSSs, we consider an open surface perpendicular to the z direction and derive an effective Hamiltonian for the HSSs near the Dirac points. We consider k_x and k_y small and decompose the BdG Hamiltonian as $\hat{H}(\mathbf{k}) = \hat{H}(0, 0, k_z) + \delta\hat{H}(k_x, k_y, 0)$. First, we derive the Dirac point energy at $k_x = k_y = 0$. At this point, $\hat{H}(0, 0, k_z)$ becomes block diagonal. This leads to $\hat{\mathcal{H}}'(0, 0, k_z) = \text{diag}(\hat{h}_{k_z,+}^{+-}, \hat{h}_{k_z,-}^{+-}, \hat{h}_{k_z,+}^{-+}, \hat{h}_{k_z,-}^{-+})$, which is identical to Eq. (6). We consider a semi-infinite system in the half space $z \geq 0$ with open boundary conditions. Therefore, k_z is no longer conserved and we treat the z direction in real space, where the momentum operator is $-i\partial_z$. The eigenvalue equation for each subblock reads $\hat{h}_{-i\partial_z,\lambda}^{\nu\nu'} \hat{\Phi}(\xi, z) = \mathcal{E}_{\text{DP}} \hat{\Phi}(\xi, z)$, where $\nu, \nu' \in \{+, -\}$ and $\hat{\Phi}(\xi, z) = (u, v)^T \exp(\xi z)$ is the trial eigenspinor of the Dirac point with ξ being its penetration length. $|u|^2$

($|v|^2$) are probability weights for electron (hole) bands having different band indices. We derive the energy of the helical topological Dirac surface points induced by unconventional FE pairing as

$$\mathcal{E}_{\text{DP}} = \pm \mu \frac{m - m'}{m + m'}, \quad (7)$$

where $m = \alpha + \beta/4$ and $m' = \alpha + 9\beta/4$ are the masses for the normal state bands. Notably, the Dirac points are tunable in energy by chemical potential μ and spin-orbit-coupling strength $m - m' = -2\beta$ [93].

Projecting the BdG Hamiltonian onto the basis of surface states results in an effective Hamiltonian for the FE helical topological surface states of the form [65]

$$\hat{H}(k_x, k_y) = (\mathcal{E}_{\text{DP}} - \varsigma_1 \mathbf{k}_{\parallel}^2) \hat{\sigma}_0 + \varsigma_2 (k_y \hat{\sigma}_x - k_x \hat{\sigma}_y), \quad (8)$$

where $\mathbf{k}_{\parallel}^2 = k_x^2 + k_y^2$, and $\varsigma_{1(2)}$ is the group velocity of the HSSs. To leading order, the HSSs exhibit the Dirac dispersion $\mathcal{E}_{\pm} \approx \mathcal{E}_{\text{DP}} \pm \varsigma_2 |\mathbf{k}_{\parallel}|$. In the limit, where either μ or $m - m'$ vanishes, the Dirac points shift to zero energy. Then, the FE helical topological surface states become dispersive helical Majorana modes [1–5]. In this case, $\hat{h}_{k_z,\pm}^{+-}$ ($\hat{h}_{k_z,\pm}^{-+}$) resembles an ordinary p -wave superconducting Hamiltonian [94]. However, for finite μ and $m - m'$, topological HSSs emerge at FE.

To identify a proper material to observe this phenomenon, certain conditions need to be satisfied. In the normal state: (i) relevant energy bands should have the same signs of curvature close to the Fermi energy, i.e., both curving downward or upward, (ii) time-reversal symmetry and twofold rotation should both be present. In the superconducting state: (i) pairing potential should be of odd-parity type, (ii) nodes should be present in the BdG spectrum at the Fermi energy such as in UTe_2 [95], (iii) nonvanishing pairing at FEs should be allowed. Candidates are antiperovskite oxides $\text{Sr}_{3-x}\text{SnO}$ [96] and half-Heusler materials $R\text{PdBi}$ with $R \in \{\text{Y}, \text{Dy}, \text{Tb}, \text{Sm}\}$ [97, 98]. Specifically, weakly hole-doped YPdBi is a promising material to observe unconventional FE Cooper pairing [97, 99]. In the SM [65], we combine density functional theory [100–103] and analytical model analysis to estimate the magnitude of FE pairing in hole-doped YPdBi [37, 65, 104]. We obtain an energy range of $\Delta_E \approx 7.7 - 46.2 \mu\text{eV}$. Notably, an energy resolution below $8 \mu\text{eV}$ at operating temperatures of 10 mK is possible via state-of-the-art STM and transport experiments in dilution refrigerators [105]. Hence, FE Cooper pairing should be observable in hole-doped YPdBi .

In addition to the materials mentioned above, hybrid structures such as $\text{BiSbTe}_{1.25}\text{Se}_{1.75}/\text{NbSe}_2$ [56, 106], and $\text{Bi}_2\text{Te}_3/\text{NbSe}_2$ [106, 107], and $X/S\text{Bi}$ with $S \in \{\text{YPt}, \text{LuPd}\}$ [60, 66, 67], and $X \in \{\text{Si}, \text{Ge}\}$ are suitable candidates for FE pairing. The excitations in Si , Ge [108], and $S\text{Bi}$ [60, 67] have $j = 3/2$ character near the Fermi energy with suitable curvature. The pairing

order parameter in SBI is believed to have p -wave septet symmetry [66, 67]. Therefore, the superconducting proximity effect of SBI to Si or Ge should induce FE pairing signaled by the emergence of HSSs.

Conclusions.— We have shown that helical topological superconducting pairing emerges in multiband time-reversal-symmetric odd-parity superconductors due to unconventional pairing away from the Fermi energy. This leads to the appearance of tunable helical topological Dirac surface states at FEs. They are topologically protected against perturbations due to combination of time-reversal and two-fold rotation symmetries [65]. Promising experimental probes are (spin-polarized) angle-resolved photoemission [109–117] and scanning tunneling spectroscopies [118–128].

The work was supported by the DFG (SPP 1666, SFB 1170 ToCoTronics, and SFB 1143, project A04, Project-Id 247310070), and the Würzburg-Dresden Cluster of Excellence ct.qmat, EXC 2147, Project-Id 390858490. We thank the Bavarian Ministry of Economic Affairs, Regional Development and Energy for financial support within the High-Tech Agenda Project “Bausteine für das Quanten Computing auf Basis topologischer Materialien”.

* masoud.bahari@physik.uni-wuerzburg.de

- [1] B. A. Bernevig, Topological insulators and topological superconductors (Princeton University Press, 2013).
- [2] M. Z. Hasan, S.-Y. Xu, and G. Bian, *Phys. Scr.* **T164**, 014001 (2015).
- [3] Y. Ando and L. Fu, *Annu. Rev. Condens. Matter Phys.* **6**, 361 (2015).
- [4] M. Sato and Y. Ando, *Rep. Prog. Phys.* **80**, 076501 (2017).
- [5] S. Shen, Topological Insulators: Dirac Equation in Condensed Matter, Springer Series in Solid-State Sciences (Springer Singapore, 2017).
- [6] L. Fu and C. L. Kane, *Phys. Rev. Lett.* **100**, 096407 (2008).
- [7] X.-L. Qi, T. L. Hughes, S. Raghu, and S.-C. Zhang, *Phys. Rev. Lett.* **102**, 187001 (2009).
- [8] M. Sato, *Phys. Rev. B.* **79**, 214526 (2009).
- [9] L. Fu and E. Berg, *Phys. Rev. Lett.* **105**, 097001 (2010).
- [10] Y. S. Hor, A. J. Williams, J. G. Checkelsky, P. Roushan, J. Seo, Q. Xu, H. W. Zandbergen, A. Yazdani, N. P. Ong, and R. J. Cava, *Phys. Rev. Lett.* **104**, 057001 (2010).
- [11] L. A. Wray, S.-Y. Xu, Y. Xia, Y. S. Hor, D. Qian, A. V. Fedorov, H. Lin, A. Bansil, R. J. Cava, and M. Z. Hasan, *Nat. Phys.* **6**, 855 (2010).
- [12] X.-L. Qi and S.-C. Zhang, *Rev. Mod. Phys.* **83**, 1057 (2011).
- [13] C. Fang, B. A. Bernevig, and M. J. Gilbert, *Phys. Rev. B* **91**, 165421 (2015).
- [14] W. Yang, Y. Li, and C. Wu, *Phys. Rev. Lett.* **117**, 075301 (2016).
- [15] Y. Wang, M. Lin, and T. L. Hughes, *Phys. Rev. B* **98**, 165144 (2018).
- [16] E. Khalaf, *Phys. Rev. B* **97**, 205136 (2018).
- [17] D. Călugăru, V. Juričić, and B. Roy, *Phys. Rev. B* **99**, 041301 (2019).
- [18] R.-X. Zhang, Y.-T. Hsu, and S. Das Sarma, *Phys. Rev. B* **102**, 094503 (2020).
- [19] R. Joynt and L. Taillefer, *Rev. Mod. Phys.* **74**, 235 (2002).
- [20] M. Sato, *Phys. Rev. B.* **73**, 214502 (2006).
- [21] B. Béri, *Phys. Rev. B.* **81**, 134515 (2010).
- [22] S. Kobayashi, K. Shiozaki, Y. Tanaka, and M. Sato, *Phys. Rev. B.* **90**, 024516 (2014).
- [23] A. P. Schnyder and P. M. R. Brydon, *J. Condens. Matter Phys.* **27**, 243201 (2015).
- [24] D. F. Agterberg, P. M. R. Brydon, and C. Timm, *Phys. Rev. Lett.* **118**, 127001 (2017).
- [25] W. Yang, T. Xiang, and C. Wu, *Phys. Rev. B.* **96**, 144514 (2017).
- [26] T. Kawakami, T. Okamura, S. Kobayashi, and M. Sato, *Phys. Rev. X* **8**, 041026 (2018).
- [27] S.-T. Tamura, S. Iimura, and S. Hoshino, *Phys. Rev. B* **102**, 024505 (2020).
- [28] A. K. Nayak, A. Steinbok, Y. Roet, J. Koo, G. Margalit, I. Feldman, A. Almoalem, A. Kanigel, G. A. Fiete, B. Yan, Y. Oreg, N. Avraham, and H. Beidenkopf, *Nat. Phys.* **17**, 1413 (2021).
- [29] A. Moreo, M. Daghofer, A. Nicholson, and E. Dagotto, *Phys. Rev. B.* **80**, 104507 (2009).
- [30] L. Komendová, A. V. Balatsky, and A. M. Black-Schaffer, *Phys. Rev. B* **92**, 094517 (2015).
- [31] C. Triola and A. V. Balatsky, *Phys. Rev. B* **95**, 224518 (2017).
- [32] J. Linder and A. V. Balatsky, *Rev. Mod. Phys.* **91**, 045005 (2019).
- [33] G. Tang, C. Bruder, and W. Belzig, *Phys. Rev. Lett.* **126**, 237001 (2021).
- [34] M. Bahari, S.-B. Zhang, and B. Trauzettel, *Phys. Rev. Research* **4**, L012017 (2022).
- [35] S. Kanasugi and Y. Yanase, *Commun. Phys.* **5**, 39 (2022).
- [36] D. Chakraborty and A. M. Black-Schaffer, *Phys. Rev. B* **106**, 024511 (2022).
- [37] P. Rüßmann, M. Bahari, S. Blügel, and B. Trauzettel, *Phys. Rev. Res.* **5**, 043181 (2023).
- [38] G. Binnig, A. Baratoff, H. E. Hoening, and J. G. Bednorz, *Phys. Rev. Lett.* **45**, 1352 (1980).
- [39] L. Shan, Y.-L. Wang, B. Shen, B. Zeng, Y. Huang, A. Li, D. Wang, H. Yang, C. Ren, Q.-H. Wang, S. H. Pan, and H.-H. Wen, *Nature Physics* **7**, 325 (2011).
- [40] X. Lin, G. Bridoux, A. Gourgout, G. Seyfarth, S. Krämer, M. Nardone, B. Fauqué, and K. Behnia, *Phys. Rev. Lett.* **112**, 207002 (2014).
- [41] S. Kittaka, Y. Aoki, Y. Shimura, T. Sakakibara, S. Seiro, C. Geibel, F. Steglich, H. Ikeda, and K. Machida, *Phys. Rev. Lett.* **112**, 067002 (2014).
- [42] T. Nomoto, K. Hattori, and H. Ikeda, *Phys. Rev. B.* **94**, 174513 (2016).
- [43] T. Nomoto and H. Ikeda, *Phys. Rev. Lett.* **117**, 217002 (2016).
- [44] K. Seo, J. D. Sau, and S. Tewari, *Phys. Rev. B.* **95**, 205107 (2017).
- [45] Y. Zhao, S. Zeng, C. Lian, Z. Dai, S. Meng, and J. Ni, *Phys. Rev. B.* **98**, 134514 (2018).
- [46] J. Singh, A. Jayaraj, D. Srivastava, S. Gayen,

- A. Thamizhavel, and Y. Singh, *Phys. Rev. B* **97**, 054506 (2018).
- [47] H. Menke, C. Timm, and P. M. R. Brydon, *Phys. Rev. B* **100**, 224505 (2019).
- [48] S. Kanasugi and Y. Yanase, *Phys. Rev. B* **100**, 094504 (2019).
- [49] C. Q. Xu, B. Li, J. J. Feng, W. H. Jiao, Y. K. Li, S. W. Liu, Y. X. Zhou, R. Sankar, N. D. Zhigadlo, H. B. Wang, Z. D. Han, B. Qian, W. Ye, W. Zhou, T. Shiroka, P. K. Biswas, X. Xu, and Z. X. Shi, *Phys. Rev. B* **100**, 134503 (2019).
- [50] J. L. Lado and M. Sigrist, *Phys. Rev. Research* **1**, 033107 (2019).
- [51] L.-H. Hu, P. D. Johnson, and C. Wu, *Phys. Rev. Research* **2**, 022021 (2020).
- [52] C. Timm and A. Bhattacharya, *Phys. Rev. B* **104**, 094529 (2021).
- [53] T. Shang, W. Xie, J. Z. Zhao, Y. Chen, D. J. Gawryluk, M. Medarde, M. Shi, H. Q. Yuan, E. Pomjakushina, and T. Shiroka, *Phys. Rev. B* **103**, 184517 (2021).
- [54] Z. Wang, S. Zeng, Y. Zhao, X. Wang, and J. Ni, *Phys. Rev. B* **104**, 174519 (2021).
- [55] C. Sevik, J. Bekaert, M. Petrov, and M. V. Milošević, *Phys. Rev. Materials* **6**, 024803 (2022).
- [56] A. Banerjee, A. Sundaresan, R. Ganesan, and P. S. A. Kumar, *ACS Nano* **12**, 12665 (2018).
- [57] H. Li, T. Zhou, J. He, H.-W. Wang, H. Zhang, H.-C. Liu, Y. Yi, C. Wu, K. T. Law, H. He, and J. Wang, *Phys. Rev. B* **96**, 075107 (2017).
- [58] J. M. Luttinger and W. Kohn, *Phys. Rev.* **97**, 869 (1955).
- [59] G. Dresselhaus, *Phys. Rev.* **100**, 580 (1955).
- [60] P. M. R. Brydon, L. Wang, M. Weinert, and D. F. Agterberg, *Phys. Rev. Lett.* **116**, 177001 (2016).
- [61] The O(3) symmetry-broken case in the normal state is analyzed in the Supplemental Material [65]
- [62] L. Savary, J. Ruhman, J. W. F. Venderbos, L. Fu, and P. A. Lee, *Phys. Rev. B* **96**, 214514 (2017).
- [63] J. W. F. Venderbos, L. Savary, J. Ruhman, P. A. Lee, and L. Fu, *Phys. Rev. X* **8**, 011029 (2018).
- [64] J. Yu and C.-X. Liu, *Phys. Rev. B* **98**, 104514 (2018).
- [65] See Supplemental Material for additional information about the reasons for TPTs at FE, properties of pseudospin rotation symmetry, global symmetries and an alternative topological index in terms of parity symmetry, O(3) symmetry-broken case and group theoretical analysis, stability of topological surface states under perturbations, derivation of helical Dirac surface states at FEs, the effective surface Hamiltonian, the FE pairing in weakly hole-doped YPdBi, and the pairing matrices in cubic symmetry. The Supplemental Material includes Refs. [13, 14, 24–27, 34, 37, 52, 60, 62–64, 67, 82–86, 97, 100–105].
- [66] H. Kim, K. Wang, Y. Nakajima, R. Hu, S. Ziemak, P. Syers, L. Wang, H. Hodovanets, J. D. Denlinger, P. M. R. Brydon, D. F. Agterberg, M. A. Tanatar, R. Prozorov, and J. Paglione, *Sci. Adv.* **4**, eaao4513 (2018).
- [67] K. Ishihara, T. Takenaka, Y. Miao, Y. Mizukami, K. Hashimoto, M. Yamashita, M. Konczykowski, R. Masuki, M. Hirayama, T. Nomoto, R. Arita, O. Pavlosiuk, P. Wiśniewski, D. Kaczorowski, and T. Shibauchi, *Phys. Rev. X* **11**, 041048 (2021).
- [68] To evaluate the tight-binding calculations, we used standard lattice regularizations $k_z^2 \rightarrow 2(1 - \cos(k_z a))/a^2$ and $k_z \rightarrow \sin(k_z a)/a$ where a is the lattice constant.
- [69] The IPR is defined by $I_E = \ln(\sum_{i=1}^{8N} |\langle i|\psi\rangle|^4 / \ln(8N))$ where N is the total number of sites and $|\psi\rangle$ indicates the eigenvector associated to E . The localized (extended) boundary (bulk) states have $I_E \rightarrow 0$ (-1).
- [70] Such a coexistence establishes topological bound states in the continuum (BIC). This has been addressed in different quantum mechanical systems [129–142]. However, the emergent topological BIC induced intrinsically by FE superconducting correlations has not been reported so far.
- [71] Our table is slightly different from the results given in Ref. [62]. The details of our calculations are given explicitly in the SM [65].
- [72] The combination of time-reversal symmetry and twofold crystalline rotation symmetry has been explored in prior works [73–78]. However, to the best of our knowledge, the prediction of finite energy pairing gaps with non-trivial topology is exclusive to our study.
- [73] C. Fang and L. Fu, *Phys. Rev. B* **91**, 161105 (2015).
- [74] F. Schindler, Z. Wang, M. G. Vergniory, A. M. Cook, A. Murani, S. Sengupta, A. Y. Kasumov, R. Deblock, S. Jeon, I. Drozdov, H. Bouchiat, S. Guéron, A. Yazdani, B. A. Bernevig, and T. Neupert, *Nature Physics* **14**, 918 (2018).
- [75] C. Fang and L. Fu, *Science Advances* **5**, eaat2374 (2019).
- [76] H. Li and K. Sun, *Phys. Rev. B* **102**, 085108 (2020).
- [77] H. Li and S. Wan, *Phys. Rev. B* **104**, 045150 (2021).
- [78] J. Henke, M. Kurttutan, J. Kruthoff, and J. van Wezel, *Phys. Rev. B* **104**, L201110 (2021).
- [79] The basis elements of $\hat{H}_{\mathbf{k}}^{+-}$ under two-fold rotation about the x (y)-axis flips the orientation of the pseudospin indices $\{\uparrow, \downarrow\} \leftrightarrow \{\downarrow, \uparrow\}$ while the momentum remains intact. In our model, the pseudospin up (down) is composed of a linear combination of magnetic quantum numbers $m_j \in \{\pm 1/2, \pm 3/2\}$.
- [80] Note that $\hat{h}_{\mathbf{k},\lambda}^{-+}$ can be easily derived by substitution of $+ \leftrightarrow -$ in Eq. (5). Note that $\delta_{\mathbf{k},\lambda}^{+-}$ fulfills the symmetry relation $\delta_{\mathbf{k},\lambda}^{+-} = -\delta_{-\mathbf{k},\lambda}^{+-}$.
- [81] The BdG Hamiltonian preserves time-reversal \hat{T} , particle-hole $\hat{\mathcal{P}}$, chiral \hat{C} , and inversion $\hat{\mathcal{P}}_u$ symmetries. The symmetry operators fulfill the properties $\hat{T}^2 = -1$ and $\hat{\mathcal{P}}^2 = \hat{\mathcal{P}}_u^2 = 1$.
- [82] L. Fu and C. L. Kane, *Phys. Rev. B* **76**, 045302 (2007).
- [83] A. P. Schnyder, S. Ryu, A. Furusaki, and A. W. W. Ludwig, *Phys. Rev. B* **78**, 195125 (2008).
- [84] T. L. Hughes, E. Prodan, and B. A. Bernevig, *Phys. Rev. B* **83**, 245132 (2011).
- [85] T. Morimoto and A. Furusaki, *Phys. Rev. B* **88**, 125129 (2013).
- [86] C.-K. Chiu, J. C. Y. Teo, A. P. Schnyder, and S. Ryu, *Rev. Mod. Phys.* **88**, 035005 (2016).
- [87] M. V. Berry, *Proc. R. Soc. Lond. A. Math. Phys. Sci.* **392**, 45 (1984).
- [88] J. Zak, *Phys. Rev. Lett.* **62**, 2747 (1989).
- [89] R. Resta, *Rev. Mod. Phys.* **66**, 899 (1994).
- [90] D. Xiao, M.-C. Chang, and Q. Niu, *Rev. Mod. Phys.* **82**, 1959 (2010).
- [91] The FE topological Dirac surface states are not restricted to the A_{2u} channel. Rather, they also exist for the other pairing channels summarized in Table I. The

- TPTs at FEs happen along the C_2 axes for the E_u and T_{2u} channels, and along the C'_2 axes for the T_{2u} channel.
- [92] The Dirac points are two-fold degenerate at one surface at positive and at negative excitation energies. Considering two surfaces, we obtain the same set of Dirac points on each surface. Thus, the degeneracy is doubled as compared to the case of single surface.
- [93] Although, spin-orbit coupling is an essential ingredient for the formation of such surface states in our model, the effective masses in systems with nearly vanishing spin-orbit coupling can stem from different orbitals giving rise to non-vanishing values for $m - m'$.
- [94] A. Y. Kitaev, *Phys-usp.* **44**, 131 (2001).
- [95] T. Metz, S. Bae, S. Ran, I.-L. Liu, Y. S. Eo, W. T. Fuhrman, D. F. Agterberg, S. M. Anlage, N. P. Butch, and J. Paglione, *Phys. Rev. B* **100**, 220504 (2019).
- [96] M. Oudah, A. Ikeda, J. N. Hausmann, S. Yonezawa, T. Fukumoto, S. Kobayashi, M. Sato, and Y. Maeno, *Nat. Commun.* **7**, 13617 (2016).
- [97] Y. Nakajima, R. Hu, K. Kirshenbaum, A. Hughes, P. Syers, X. Wang, K. Wang, R. Wang, S. R. Saha, D. Pratt, J. W. Lynn, and J. Paglione, *Sci. Adv.* **1**, e1500242 (2015).
- [98] The inversion breaking anti-symmetric spin-orbit-coupling (ASOC) in half-Heusler material is weak compared to symmetric spin-orbit coupling.
- [99] S. M. A. Radmanesh, C. Martin, Y. Zhu, X. Yin, H. Xiao, Z. Q. Mao, and L. Spinu, *Phys. Rev. B* **98**, 241111 (2018).
- [100] P. Růřmann, D. Antognini Silva, D. S. G. Bauer, P. Baumeister, P. F. Bornemann, J. Bouaziz, S. Brinker, J. Chico, P. H. Dederichs, B. H. Drittlter, F. Dos Santos, M. dos Santos Dias, N. Essing, G. Geranton, I. Klepetsanis, A. Kosma, N. H. Long, S. Lounis, P. Mavropoulos, E. Mendive Tapia, C. Oran, N. Papanikolaou, E. Rabel, B. Schweffinghaus, N. Stefanou, A. R. Thiess, R. Zeller, B. Zimmermann, and S. Blügel, “Judftteam/jukkr: v3.6,” (2022).
- [101] P. Růřmann and S. Blügel, *Phys. Rev. B* **105**, 125143 (2022).
- [102] A. Jain, S. P. Ong, G. Hautier, W. Chen, W. D. Richards, S. Dacek, S. Cholia, D. Gunter, D. Skinner, G. Ceder, and K. A. Persson, *APL Materials* **1**, 011002 (2013).
- [103] W. L. Vosko, S. H. and N. M., *Can. J. Phys.* **58** (1980), 10.1139/p80-159.
- [104] V. Bhardwaj, A. Bhattacharya, S. Srivastava, V. V. Khovaylo, J. Sannigrahi, N. Banerjee, B. K. Mani, and R. Chatterjee, *Sci. Rep.* **11**, 7535 (2021).
- [105] J. Schwenk, S. Kim, J. Berwanger, F. Ghahari, D. Walkup, M. R. Slot, S. T. Le, W. G. Cullen, S. R. Blankenship, S. Vranjkovic, H. J. Hug, Y. Kuk, F. J. Giessibl, and J. A. Stroscio, *Review of Scientific Instruments* **91**, 071101 (2020).
- [106] X. Xi, Z. Wang, W. Zhao, J.-H. Park, K. T. Law, H. Berger, L. Forró, J. Shan, and K. F. Mak, *Nature Physics* **12**, 139 (2016).
- [107] H. Zhang, C.-X. Liu, X.-L. Qi, X. Dai, Z. Fang, and S.-C. Zhang, *Nature Physics* **5**, 438 (2009).
- [108] M. Grundmann, *The Physics of Semiconductors: An Introduction Including Devices and Nanophysics* (Springer, Berlin Heidelberg, 2006).
- [109] D. Hsieh, Y. Xia, L. Wray, D. Qian, A. Pal, J. H. Dil, J. Osterwalder, F. Meier, G. Bihlmayer, C. L. Kane, Y. S. Hor, R. J. Cava, and M. Z. Hasan, *Science* **323**, 919 (2009).
- [110] Y. Zhang, L. X. Yang, M. Xu, Z. R. Ye, F. Chen, C. He, H. C. Xu, J. Jiang, B. P. Xie, J. J. Ying, X. F. Wang, X. H. Chen, J. P. Hu, M. Matsunami, S. Kimura, and D. L. Feng, *Nat. Mater.* **10**, 273 (2011).
- [111] D. V. Evtushinsky, V. B. Zabolotnyy, T. K. Kim, A. A. Kordyuk, A. N. Yaresko, J. Maletz, S. Aswartham, S. Wurmehl, A. V. Boris, D. L. Sun, C. T. Lin, B. Shen, H. H. Wen, A. Varykhalov, R. Follath, B. Büchner, and S. V. Borisenko, *Phys. Rev. B.* **89**, 064514 (2014).
- [112] E. J. Sie, T. Rohwer, C. Lee, and N. Gedik, *Nat. Commun.* **10**, 3535 (2019).
- [113] J. J. P. Thompson, D. Pei, H. Peng, H. Wang, N. Channa, H. L. Peng, A. Barinov, N. B. M. Schröter, Y. Chen, and M. Mucha-Kruczyński, *Nat. Commun.* **11**, 3582 (2020).
- [114] W. Liu, L. Cao, S. Zhu, L. Kong, G. Wang, M. Papaj, P. Zhang, Y.-B. Liu, H. Chen, G. Li, F. Yang, T. Kondo, S. Du, G.-H. Cao, S. Shin, L. Fu, Z. Yin, H.-J. Gao, and H. Ding, *Nat. Commun.* **11**, 5688 (2020).
- [115] C. Liu, R. P. Day, F. Li, R. L. Roemer, S. Zhdanovich, S. Gorovikov, T. M. Pedersen, J. Jiang, S. Lee, M. Schneider, D. Wong, P. Dosanjh, F. J. Walker, C. H. Ahn, G. Levy, A. Damascelli, G. A. Sawatzky, and K. Zou, *Nat. Commun.* **12**, 4573 (2021).
- [116] C. Lin, M. Ochi, R. Noguchi, K. Kuroda, M. Sakoda, A. Nomura, M. Tsubota, P. Zhang, C. Bareille, K. Kurokawa, Y. Arai, K. Kawaguchi, H. Tanaka, K. Yaji, A. Harasawa, M. Hashimoto, D. Lu, S. Shin, R. Arita, S. Tanda, and T. Kondo, *Nat. Mater.* **20**, 1093 (2021).
- [117] S.-D. Chen, M. Hashimoto, Y. He, D. Song, J.-F. He, Y.-F. Li, S. Ishida, H. Eisaki, J. Zaanen, T. P. Devereaux, D.-H. Lee, D.-H. Lu, and Z.-X. Shen, *Nature*. **601**, 562 (2022).
- [118] M. Bode, *Rep. Prog. Phys* **66**, 523 (2003).
- [119] J. Wiebe, A. Wachowiak, F. Meier, D. Haude, T. Foster, M. Morgenstern, and R. Wiesendanger, *Rev. Sci. Instrum.* **75**, 4871 (2004).
- [120] Z. Alpichshev, J. G. Analytis, J.-H. Chu, I. R. Fisher, Y. L. Chen, Z. X. Shen, A. Fang, and A. Kapitulnik, *Phys. Rev. Lett.* **104**, 016401 (2010).
- [121] O. Fischer, M. Kugler, I. Maggio-Aprile, C. Berthod, and C. Renner, *Rev. Mod. Phys.* **79**, 353 (2007).
- [122] H. Oka, O. O. Brovko, M. Corbetta, V. S. Stepanyuk, D. Sander, and J. Kirschner, *Rev. Mod. Phys.* **86**, 1127 (2014).
- [123] M. Neupane, N. Alidoust, M. M. Hosen, J.-X. Zhu, K. Dimitri, S.-Y. Xu, N. Dhakal, R. Sankar, I. Belopolski, D. S. Sanchez, T.-R. Chang, H.-T. Jeng, K. Miyamoto, T. Okuda, H. Lin, A. Bansil, D. Kaczorowski, F. Chou, M. Z. Hasan, and T. Durakiewicz, *Nat. Commun.* **7**, 13315 (2016).
- [124] L. Cornils, A. Kamlapure, L. Zhou, S. Pradhan, A. A. Khajetoorians, J. Fransson, J. Wiebe, and R. Wiesendanger, *Phys. Rev. Lett.* **119**, 197002 (2017).
- [125] D.-J. Choi, C. Rubio-Verdú, J. de Bruijckere, M. M. Ugeda, N. Lorente, and J. I. Pascual, *Nat. Commun.* **8**, 15175 (2017).
- [126] P. Fan, F. Yang, G. Qian, H. Chen, Y.-Y. Zhang, G. Li, Z. Huang, Y. Xing, L. Kong, W. Liu, K. Jiang, C. Shen, S. Du, J. Schneeloch, R. Zhong, G. Gu, Z. Wang, H. Ding, and H.-J. Gao, *Nat. Commun.* **12**, 1348

- (2021).
- [127] D. Wang, J. Wiebe, R. Zhong, G. Gu, and R. Wiesendanger, *Phys. Rev. Lett.* **126**, 076802 (2021).
- [128] L. Schneider, P. Beck, J. Wiebe, and R. Wiesendanger, *Sci. Adv.* **7**, eabd7302 (2021).
- [129] Y. Plotnik, O. Peleg, F. Dreisow, M. Heinrich, S. Nolte, A. Szameit, and M. Segev, *Phys. Rev. Lett.* **107**, 183901 (2011).
- [130] J. Mur-Petit and R. A. Molina, *Phys. Rev. B.* **90**, 035434 (2014).
- [131] Y. Baum, T. Posske, I. C. Fulga, B. Trauzettel, and A. Stern, *Phys. Rev. Lett.* **114**, 136801 (2015).
- [132] C. W. Hsu, B. Zhen, A. D. Stone, J. D. Joannopoulos, and M. Soljavic, *Nat. Rev. Mater.* **1**, 16048 (2016).
- [133] L. S. Ricco, Y. Marques, F. A. Dessotti, R. S. Machado, M. de Souza, and A. C. Seridonio, *Phys. Rev. B.* **93**, 165116 (2016).
- [134] Y.-X. Xiao, G. Ma, Z.-Q. Zhang, and C. T. Chan, *Phys. Rev. Lett.* **118**, 166803 (2017).
- [135] S. Mukherjee, J. Gomis-Bresco, P. Pujol-Closa, D. Artigas, and L. Torner, *Phys. Rev. A.* **98**, 063826 (2018).
- [136] M. Bahari and M. V. Hosseini, *Phys. Rev. B.* **99**, 155128 (2019).
- [137] M. Takeichi and S. Murakami, *Phys. Rev. B.* **99**, 035128 (2019).
- [138] Z.-G. Chen, C. Xu, R. Al Jahdali, J. Mei, and Y. Wu, *Phys. Rev. B.* **100**, 075120 (2019).
- [139] M. Jangjan and M. V. Hosseini, *Sci. Rep.* **10**, 14256 (2020).
- [140] W. A. Benalcazar and A. Cerjan, *Phys. Rev. B.* **101**, 161116 (2020).
- [141] A. Cerjan, M. Jürgensen, W. A. Benalcazar, S. Mukherjee, and M. C. Rechtsman, *Phys. Rev. Lett.* **125**, 213901 (2020).
- [142] Z. Gong, J. Serafini, F. Yang, S. Preble, and J. Yao, *Phys. Rev. Applied* **16**, 024059 (2021).

Supplemental Material

In this section, we address why TPTs at FEs occur only in odd-parity multiband superconductors with time-reversal symmetry. We show that the FE pairing potential is odd under the parity operation. To this end, we start by examining the parity and time-reversal symmetry properties of the normal state and the pairing potential. A fermionic state $|\mathbf{k}, m_j\rangle$, with \mathbf{k} as the 3D momentum, and m_j being the magnetic quantum number of total angular momentum j , transforms under inversion P and time-reversal T operations, respectively, as

$$P|\mathbf{k}, m_j\rangle = |-\mathbf{k}, m_j\rangle, \quad (9)$$

$$T|\mathbf{k}, m_j\rangle = (-1)^{j+m_j} |-\mathbf{k}, -m_j\rangle. \quad (10)$$

Inversion symmetry acts only on the momenta and the magnetic quantum number remains intact. In this case, the matrix form of the inversion operator is a 4×4 identity matrix. The matrix representation of the anti-unitary time-reversal operator takes the form $\hat{T} = \hat{\mathcal{R}}\mathcal{K}$ with \mathcal{K} being the complex conjugation and the unitary part $\hat{\mathcal{R}} = e^{i\pi\hat{J}_y} = i\hat{\sigma}_x \otimes \hat{\sigma}_y$.

The normal state preserves inversion and time-reversal symmetries described by

$$\hat{P}\hat{\mathcal{H}}_{\mathbf{k}}\hat{P}^{-1} = \hat{\mathcal{H}}_{-\mathbf{k}}, \quad \hat{\mathcal{R}}\hat{\mathcal{H}}_{\mathbf{k}}^*\hat{\mathcal{R}}^{-1} = \hat{\mathcal{H}}_{-\mathbf{k}}. \quad (11)$$

Moreover, the normal state preserves the combination of these symmetries given by $(\hat{P}\hat{T})\hat{\mathcal{H}}_{\mathbf{k}}(\hat{P}\hat{T})^{-1} = \hat{\mathcal{H}}_{\mathbf{k}}$ leading to doubly degenerate eigenstates.

The parity of a pairing potential is distinguished by the orbital angular momentum of Cooper pairing, i.e., $L = 2n + 1$ ($L = 2n$) denotes odd- (even-) parity angular momenta with n being non-negative integers. In this case, the pairing potential is odd u (even g) under the parity operation given by

$$\hat{P}\hat{\Delta}_{\mathbf{k}}\hat{P}^{-1} = -(+)\hat{\Delta}_{-\mathbf{k}}. \quad (12)$$

We can show that the BdG Hamiltonian, given in Eq. (1) of the main paper, satisfies inversion symmetry for odd- (even-) parity pairing potential given by

$$\hat{\mathcal{P}}_{u,g}\hat{H}(\mathbf{k})\hat{\mathcal{P}}_{u,g}^{-1} = \hat{H}(-\mathbf{k}), \quad (13)$$

where $\hat{\mathcal{P}}_u = \hat{\sigma}_z \otimes \hat{P}$ and $\hat{\mathcal{P}}_g = \hat{\sigma}_0 \otimes \hat{P}$. Furthermore, a pairing potential is time-reversal symmetric described by

$$\hat{\mathcal{R}}\hat{\Delta}_{\mathbf{k}}^*\hat{\mathcal{R}}^{-1} = \hat{\Delta}_{-\mathbf{k}} = \pm\hat{\Delta}_{\mathbf{k}}, \quad (14)$$

where $-(+)$ corresponds to odd- (even-) parity pairing potentials. In our investigations, we focus on odd-parity pairing potentials which preserve time-reversal symmetry.

Due to inversion symmetry in the normal state, the pseudospin operator $\hat{V}_{\mathbf{k}} = \{\hat{V}_{\mathbf{k}}^+, \hat{V}_{\mathbf{k}}^-\}$ is an even-parity matrix function, i.e., $\hat{V}_{\mathbf{k}}^{\pm} = \hat{V}_{-\mathbf{k}}^{\pm}$. It is given explicitly by

$$\hat{V}_{\mathbf{k}}^+ = \frac{1}{2} \frac{|\mathbf{k}_{||}|}{|\mathbf{k}|} \begin{pmatrix} 2k_z k_- / k_+^2 & k_- / k_+ \\ \sqrt{3} k_- / k_+ & 0 \\ 0 & \sqrt{3} \\ 1 & -2k_z / k_- \end{pmatrix}, \quad (15)$$

and

$$\hat{V}_{\mathbf{k}}^- = \frac{1}{\Gamma_{\mathbf{k}}^-} \begin{pmatrix} 2\sqrt{3}k_z k_- \mathbf{k}_{||}^2 / k_+^2 & -\sqrt{3}k_-^2 \\ -(|\mathbf{k}|^2 + 3k_z^2) \mathbf{k}_{||}^2 / k_+^2 & 0 \\ 0 & |\mathbf{k}|^2 + 3k_z^2 \\ \sqrt{3}\mathbf{k}_{||}^2 & 2\sqrt{3}k_z k_+ \end{pmatrix}, \quad (16)$$

where $\mathbf{k}_{||}^2 = k_x^2 + k_y^2$, $\Gamma_{\mathbf{k}}^- = 2|\mathbf{k}|\sqrt{|\mathbf{k}|^2 + 3k_z^2}$, $|\mathbf{k}| = \sqrt{\mathbf{k}_{||}^2 + k_z^2}$, and $k_{\pm} = k_x \pm ik_y$.

The parity of the pairing potential projected onto the pseudospin basis, i.e., $\hat{\Delta}_{\mathbf{k}}^{\nu\nu'}$ with $\nu\nu' \in \{+, -\}$, is the same as the parity of the unprojected pairing potential.

We prove this by the symmetry relation

$$\begin{aligned}
\hat{\mathfrak{P}}\hat{\Delta}_{\mathbf{k}}^{\nu\nu'}\hat{\mathfrak{P}}^{-1} &= \hat{\mathfrak{P}}\hat{V}_{\mathbf{k}}^{\nu\nu'}\hat{\Delta}_{\mathbf{k}}(\hat{V}_{-\mathbf{k}}^{\nu'\dagger})^T\hat{\mathfrak{P}}^{-1} \\
&= \hat{\mathfrak{P}}\hat{V}_{\mathbf{k}}^{\nu\nu'}(\pm\hat{P}^{-1}\hat{\Delta}_{-\mathbf{k}}\hat{P})(\hat{V}_{-\mathbf{k}}^{\nu'\dagger})^T\hat{\mathfrak{P}}^{-1} \\
&= \pm\hat{V}_{-\mathbf{k}}^{\nu\nu'}\hat{\Delta}_{-\mathbf{k}}(\hat{V}_{+\mathbf{k}}^{\nu'\dagger})^T \\
&= \pm\hat{V}_{\mathbf{k}}^{\nu\nu'}\hat{\Delta}_{-\mathbf{k}}(\hat{V}_{-\mathbf{k}}^{\nu'\dagger})^T \\
&= \pm\hat{\Delta}_{-\mathbf{k}}^{\nu\nu'}, \tag{17}
\end{aligned}$$

where $\hat{\mathfrak{P}}$ is the inversion operator defined by a 2×2 identity matrix in pseudospin basis. Note that to derive Eq. (17), we consider the even-parity property of the eigen-spinors. This shows that the inversion symmetry of the normal state is crucial to the determine the parity of the projected pairing. Therefore, the FE pairing potential, which is responsible for TPTs at FEs, has odd- (even-) parity if the orbital angular momentum of Cooper pairing is odd (even), i.e.,

$$\hat{\mathfrak{P}}\hat{\Delta}_{\mathbf{k}}^{+-}\hat{\mathfrak{P}}^{-1} = -(+)\hat{\Delta}_{-\mathbf{k}}^{+-}. \tag{18}$$

In the lattice representation, we replace even (odd) momenta in the finite energy pairing potential $\hat{\Delta}_{k_\nu}^{+-}$ by

$$k_\nu^{2n+1} \rightarrow [2(1 - \cos(k_\nu))]^n \sin(k_\nu), \quad \text{for } L = \text{odd}, \tag{19}$$

$$k_\nu^{2n} \rightarrow [2(1 - \cos(k_\nu))]^n, \quad \text{for } L = \text{even}, \tag{20}$$

where $\nu \in \{x, y, z\}$ and we assume the lattice constant to be unity. The odd-parity pairing channels contain odd powers of momenta in $\hat{\Delta}_{\mathbf{k}}^{+-}$ along the TPTs direction. Thus, the $\sin(k_\nu)$ term in Eq. (19) forces $\hat{\Delta}_{k_\nu=\pm\pi}^{+-} = 0$ at the parity-time-reversal-invariant momenta (PTRIM), i.e., $k_\nu = \pm\pi$. This allows to close and reopen the gap, through the manipulation of the normal state parameters at FEs. Therefore, helical Dirac surface states emerge only for the odd-parity pairing channels.

In contrast, bulk bands for even-parity pairing channels at FEs never close at $k_\nu = \pm\pi$, i.e., $\hat{\Delta}_{k_\nu=\pm\pi}^{+-} = 4^n \neq 0$. This prohibits the quantization of the topological index. Therefore, the system remains in the topologically trivial phase.

We illustrate the aforementioned general argument by two examples. Since we focus on the p -wave pairing channel, the momenta appear in linear order, i.e., $L = 1$ ($n = 0$). Consider the A_{2u} pairing along the direction $\mathbf{k} = (0, 0, k_z)$. The BdG Hamiltonian is block diagonal through the unitary transformation constructed from $\hat{D}_{\mathbf{n}}(\pi, \epsilon)$ symmetry in the interband basis, i.e., $\hat{\mathcal{H}}''(0, 0, k_z) = \text{diag}(\hat{h}_{k_z, +}^-, \hat{h}_{k_z, +}^+, \hat{h}_{k_z, -}^+, \hat{h}_{k_z, -}^-)$. The explicit matrix form of $\hat{h}_{k_z, \pm}^{\pm}$ in the lattice representation is

$$\hat{h}_{k_z, \pm}^{\pm} = \begin{pmatrix} -E_{k_z}^- & \Delta \sin(k_z) \\ \Delta \sin(k_z) & E_{k_z}^+ \end{pmatrix}, \tag{21}$$

where the off-diagonal terms correspond to the FE pairing. In Eq. (21), $-E_{k_z}^-$ ($E_{k_z}^+$) is the hole (electron) band given by

$$E_{k_z}^- = 2(\alpha + \beta/4)(1 - \cos(k_z)) - \mu, \tag{22}$$

$$E_{k_z}^+ = 2(\alpha + 9\beta/4)(1 - \cos(k_z)) - \mu. \tag{23}$$

The TPT occurs at the PTRIM $\mathbf{k} = (0, 0, \pm\pi)$ where the spectrum of Eq. (21) becomes

$$\varepsilon_1 = \mu - (4\alpha + \beta), \quad \varepsilon_2 = 4\alpha + 9\beta - \mu. \tag{24}$$

We assume the normal state energy bands to have identical sign of curvature, i.e., $\text{sgn}(\alpha) = \text{sgn}(\beta) = \pm 1$. In this case, the system exhibits a gap at $\mathbf{k} = (0, 0, \pm\pi)$, i.e., $|\varepsilon_1 - \varepsilon_2| = 2|4\alpha + 9\beta - \mu| > 0$. The TPT occurs when $|\varepsilon_1 - \varepsilon_2| = 0$. This results in the phase transition relation $\mu = 4\alpha + 9\beta$. Hence, the TPT at nonzero excitation energies can occur through the interplay between odd-parity superconductivity and normal state crossings at finite excitation energies.

In realistic materials, α and β are fixed and the system can exhibit a topological phase for a certain range of chemical potentials. This is illustrated by the topological phase diagram in Fig. 1(c) in the main text.

In contrast, the FE pairing never vanishes at PTRIM for even-parity pairing channels. To illustrate this, consider the even-parity s -wave E_g pairing given by the pairing matrix $\hat{\Delta}_{\mathbf{k}} = (\Delta/3)(2\hat{j}_z^2 - \hat{j}_x^2 - \hat{j}_y^2)\hat{\mathcal{R}}$ [24]. This pairing matrix exhibits vanishing (nonvanishing) intra- (inter-) band pairing at momenta $2k_z^2 = k_x^2 + k_y^2$, i.e., $\hat{\Delta}_{\mathbf{k}}^{\text{intra}} = 0$ and $\hat{\Delta}_{\mathbf{k}}^{\text{inter}} \neq 0$. Therefore, this instability channel is a candidate for the TPTs at FEs. The FE pairing is even under the parity exchange, i.e., $\hat{\mathfrak{P}}\hat{\Delta}_{\mathbf{k}}^{+-}\hat{\mathfrak{P}}^{-1} = \hat{\Delta}_{-\mathbf{k}}^{+-}$ with $\hat{\Delta}_{\mathbf{k}}^{\pm} = \Delta(k_+/k_-)\hat{\tau}_x$ where $k_{\pm} = k_x \pm ik_y$. In this case, the interband superconducting Hamiltonian becomes

$$\hat{H}_{\mathbf{k}}^{+-} = \begin{pmatrix} E_{\mathbf{k}}^+ \hat{\tau}_0 & \Delta(k_+/k_-)\hat{\tau}_x \\ \Delta(k_-/k_+)\hat{\tau}_x & -E_{\mathbf{k}}^- \hat{\tau}_0 \end{pmatrix}, \tag{25}$$

where

$$E_{\mathbf{k}}^+ = (3/8)(4\alpha + 9\beta)(k_x^2 + k_y^2) - \mu, \tag{26}$$

$$E_{\mathbf{k}}^- = (3/8)(4\alpha + \beta)(k_x^2 + k_y^2) - \mu. \tag{27}$$

Equation (25) preserves a rotational symmetry along the z -axis in pseudospin basis with rotation angle $\theta = \pi$ given by $\hat{D}_{\mathbf{n}_z}(\pi, 1) = \text{diag}(i\hat{\tau}_z, -i\hat{\tau}_z)$. Therefore, $\hat{H}_{\mathbf{k}}^{+-}$ becomes diagonal in the eigenbasis of $\hat{D}_{\mathbf{n}_z}(\pi, 1)$ labeled by eigenvalues $\lambda = \pm i$ obtained by $\hat{U}^\dagger \hat{H}_{\mathbf{k}}^{+-} \hat{U} = \text{diag}(\hat{h}_{\mathbf{k}, +i}^+, \hat{h}_{\mathbf{k}, -i}^-)$ with

$$\hat{h}_{\mathbf{k}, \pm i}^{\pm} = \begin{pmatrix} -E_{\mathbf{k}}^- & \Delta(k_-/k_+) \\ \Delta(k_+/k_-) & E_{\mathbf{k}}^+ \end{pmatrix}, \tag{28}$$

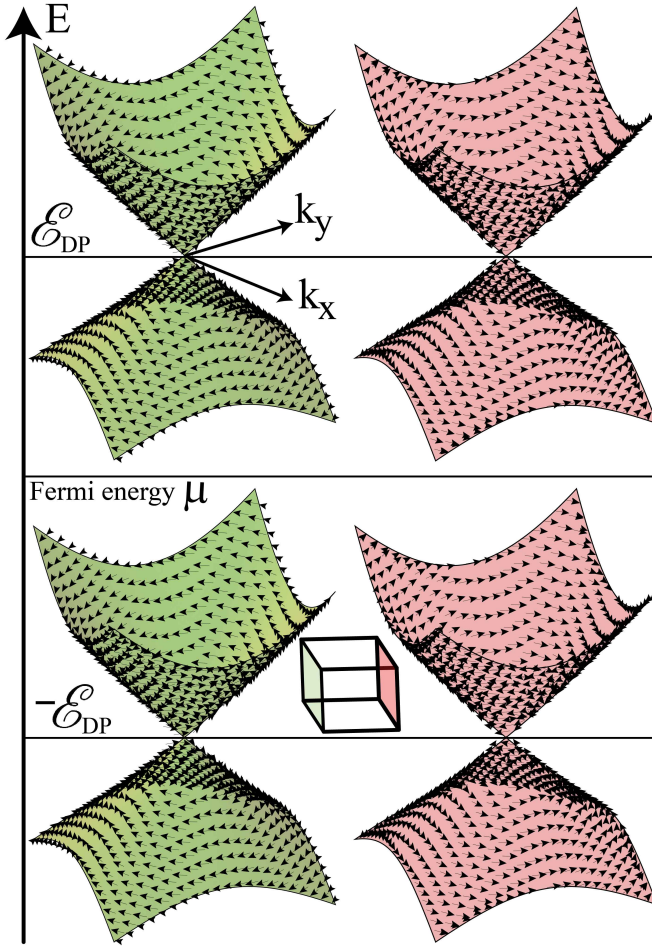


Figure 3. Helical topological Dirac cones at finite excitation energies induced by FE Cooper pairing. A pair of helical Dirac cones (pink) emerge on a surface and the degenerate partner appears on the other surface (green). Black arrows illustrate the spin texture of the surface states exhibiting spin-momentum locking due to the helical property. \mathcal{E}_{DP} denotes energy of the Dirac points and μ is the Fermi energy of the normal state.

where the matrix of eigenvectors for $\hat{D}_{\mathbf{n}_z}(\pi, 1)$ is given by

$$\hat{U} = \begin{pmatrix} 0 & 1 & 0 & 0 \\ 0 & 0 & 0 & 1 \\ 0 & 0 & 1 & 0 \\ 1 & 0 & 0 & 0 \end{pmatrix}. \quad (29)$$

The spectrum of Eq. (28) is always gapped at FEs. Hence, TPTs at FEs are not possible.

Appendix A: Pseudospin rotation symmetry properties

In this section, we explain the constraint imposed by pseudospin rotation symmetry on the FE pairing potential. The motivation behind such analysis is to show the

explicit form of a general FE pairing matrix fulfilling the pseudospin rotation symmetry. To this end, we present the FE pairing matrix in a general form

$$\hat{\Delta}_{\mathbf{k}}^{+-} \equiv \mathbf{g}_{\mathbf{k}} \cdot \hat{\boldsymbol{\tau}}, \quad (A1)$$

where the four-component $\mathbf{g}_{\mathbf{k}}$ vector is given by $\mathbf{g}_{\mathbf{k}} = (\mathbf{g}_0, \mathbf{g}_x, \mathbf{g}_y, \mathbf{g}_z)$ with the components being momentum dependent functions (this dependency is dropped). The four-component vector of Pauli matrices is defined in the interband basis by $\hat{\boldsymbol{\tau}} = (\hat{\tau}_0, \hat{\tau}_x, \hat{\tau}_y, \hat{\tau}_z)$ with $\hat{\tau}_0$ being a 2×2 identity matrix.

The matrix representation of FE pairing potential converts to a pairing function $\delta_{\mathbf{k},\lambda}^{+-}$ (see Eq. (5) in the main text) in the presence of $\hat{D}_{\mathbf{n}}(\pi, \epsilon)$ symmetry where the rotation angle is about the arbitrary unit vector $\mathbf{n} = (n_x, n_y, n_z)$. In this case, the relation between $\hat{\Delta}_{\mathbf{k}}^{+-}$ and $\delta_{\mathbf{k},\lambda}^{+-}$ can be distinguished by the components of the vector $\mathbf{g}_{\mathbf{k}}$. Interestingly, the pseudospin rotation symmetry about the x(y)[z] axis, defined by

$$\mathbf{n}_x \equiv (1, 0, 0), \quad \mathbf{n}_y \equiv (0, 1, 0), \quad \mathbf{n}_z \equiv (0, 0, 1), \quad (A2)$$

enforces $\delta_{\mathbf{k},\lambda}^{+-}$ to select up to two components of the vector $\mathbf{g}_{\mathbf{k}}$. After some algebra, such constraints for the $\epsilon = -1$ representation can be obtained by

$$[\hat{D}_{\mathbf{n}_z}(\pi, -1), \hat{H}_{\mathbf{k}}^{+-}] = 0 \rightarrow \delta_{\mathbf{k},\lambda}^{+-} = \mathbf{g}_0 + \lambda \mathbf{g}_z, \quad (A3)$$

$$[\hat{D}_{\mathbf{n}_y}(\pi, -1), \hat{H}_{\mathbf{k}}^{+-}] = 0 \rightarrow \delta_{\mathbf{k},\lambda}^{+-} = \lambda i \mathbf{g}_x - \mathbf{g}_z, \quad (A4)$$

$$[\hat{D}_{\mathbf{n}_x}(\pi, -1), \hat{H}_{\mathbf{k}}^{+-}] = 0 \rightarrow \delta_{\mathbf{k},\lambda}^{+-} = \mathbf{g}_0 + \lambda \mathbf{g}_x. \quad (A5)$$

To interpret the above relations, we consider Eq. (A3) as an example. In this case, $\delta_{\mathbf{k},\lambda}^{+-}$ preserves the pseudospin rotation symmetry under the rotation angle $\theta = \pi$ about the z-axis if either \mathbf{g}_0 or \mathbf{g}_z , or both of them are finite, and the other components vanish, i.e., $\mathbf{g}_{\mathbf{k}} = (\mathbf{g}_0, 0, 0, \mathbf{g}_z)$. This is a useful result since we can directly ascertain the pseudospin rotation symmetry of a FE pairing potential in multiband superconductors by checking only the components of the vector $\mathbf{g}_{\mathbf{k}}$.

The dot product of the vector $\mathbf{g}_{\mathbf{k}}$ and the Pauli matrices in Eq. (A1) allows us to find the relation between $\hat{\Delta}_{\mathbf{k}}^{+-}$ and a proper $\hat{D}_{\mathbf{n}}(\pi, \epsilon)$ symmetry given by

$$\hat{D}_{\mathbf{n}_z}(\pi, -1) : \hat{\Delta}_{\mathbf{k}}^{+-} = \mathbf{g}_0 \hat{\tau}_0 + \mathbf{g}_z \hat{\tau}_z, \quad (A6)$$

$$\hat{D}_{\mathbf{n}_y}(\pi, -1) : \hat{\Delta}_{\mathbf{k}}^{+-} = \mathbf{g}_x \hat{\tau}_x + \mathbf{g}_z \hat{\tau}_z, \quad (A7)$$

$$\hat{D}_{\mathbf{n}_x}(\pi, -1) : \hat{\Delta}_{\mathbf{k}}^{+-} = \mathbf{g}_0 \hat{\tau}_0 + \mathbf{g}_x \hat{\tau}_x. \quad (A8)$$

Importantly, we observe that the component \mathbf{g}_y in Eqs. (A3-A8) is absent. However, the pseudospin rotation symmetry with $\epsilon = +1$ representation reveals the allowed symmetry form of $\delta_{\mathbf{k},\lambda}^{+-}$ including the y-component of $\mathbf{g}_{\mathbf{k}}$,

$$[\hat{D}_{\mathbf{n}_z}(\pi, 1), \hat{H}_{\mathbf{k}}^{+-}] = 0 \rightarrow \delta_{\mathbf{k},\lambda}^{+-} = \mathbf{g}_x - i \lambda \mathbf{g}_y, \quad (A9)$$

$$[\hat{D}_{\mathbf{n}_y}(\pi, 1), \hat{H}_{\mathbf{k}}^{+-}] = 0 \rightarrow \delta_{\mathbf{k},\lambda}^{+-} = \mathbf{g}_0 + \lambda \mathbf{g}_y, \quad (A10)$$

$$[\hat{D}_{\mathbf{n}_x}(\pi, 1), \hat{H}_{\mathbf{k}}^{+-}] = 0 \rightarrow \delta_{\mathbf{k},\lambda}^{+-} = -i \lambda \mathbf{g}_y - \mathbf{g}_z. \quad (A11)$$

In this case, the $\hat{\mathcal{D}}_{\mathbf{n}}(\pi, \epsilon)$ symmetry forces the FE pairing matrix to have the explicit form

$$\hat{\mathcal{D}}_{\mathbf{n}_z}(\pi, 1) : \hat{\Delta}_{\mathbf{k}}^{+-} = \mathbf{g}_x \hat{\tau}_x + \mathbf{g}_y \hat{\tau}_y, \quad (\text{A12})$$

$$\hat{\mathcal{D}}_{\mathbf{n}_y}(\pi, 1) : \hat{\Delta}_{\mathbf{k}}^{+-} = \mathbf{g}_0 \hat{\tau}_0 + \mathbf{g}_y \hat{\tau}_y, \quad (\text{A13})$$

$$\hat{\mathcal{D}}_{\mathbf{n}_x}(\pi, 1) : \hat{\Delta}_{\mathbf{k}}^{+-} = \mathbf{g}_y \hat{\tau}_y + \mathbf{g}_z \hat{\tau}_z. \quad (\text{A14})$$

Taking into account Eqs. (A6-A8) and (A12-A14), we can understand the explicit form of the $\hat{\mathcal{D}}_{\mathbf{n}}(\pi, \epsilon)$ symmetry along the TPT direction by looking at the components of $\hat{\Delta}_{\mathbf{k}}^{+-}$, e.g., the last column of Table. I in the main text. For instance, one of the TPT directions for the T_{2u} irrep is $\mathbf{k} \in (\pm k, 0, \pm k)$ and the FE pairing potential is given by $\hat{\Delta}_{\mathbf{k}}^{+-} = \Delta k(\pm \hat{\tau}_0/3 - i \hat{\tau}_y)$. According to Eq. (A13), $\hat{\Delta}_{\mathbf{k}}^{+-}$ preserves $\hat{\mathcal{D}}_{\mathbf{n}_y}(\pi, 1)$ symmetry with $\mathbf{g}_0 = \pm \Delta k/3$ and $\mathbf{g}_y = \pm i \Delta k$.

Note that when $\hat{\Delta}_{\mathbf{k}}^{+-}$ contains only one component of $\mathbf{g}_{\mathbf{k}}$ along the TPT direction, the rotation axis of the $\hat{\mathcal{D}}_{\mathbf{n}}(\pi, \epsilon)$ is not unique. Importantly, the momentum dependency of components of the $\mathbf{g}_{\mathbf{k}}$ along the TPT direction is proportional to the orbital angular momentum of Cooper pairing. For instance, $\mathbf{g}_{\mathbf{k}}$ is proportional to linear order of momenta at TPT directions since we focus on p -wave pairing, i. e., $L = 1$.

The reason for having two representations for the $\hat{\mathcal{D}}_{\mathbf{n}}(\pi, \epsilon)$ symmetry can be seen by the unitary transformation $\hat{\mathcal{V}}$ between the eigenbases for $\epsilon = +1$ and $\epsilon = -1$,

$$\hat{\phi}_{+1} = \hat{\mathcal{V}} \hat{\phi}_{-1}, \quad \hat{\mathcal{V}} = \hat{\mathcal{V}}^{-1} = \hat{\mathcal{V}}^\dagger = \begin{pmatrix} 0 & 0 & 1 & 0 \\ 0 & 1 & 0 & 0 \\ 1 & 0 & 0 & 0 \\ 0 & 0 & 0 & 1 \end{pmatrix}, \quad (\text{A15})$$

where $\hat{\phi}_{\epsilon=\pm 1} = \hat{U}^{-1} \hat{\phi}_{\mathbf{k}}^{+-}$ with $\hat{\phi}_{\mathbf{k}}^{+-}$ being the 4×1 column as the basis of FE superconducting Hamiltonian $\hat{H}_{\mathbf{k}}^{+-}$, and \hat{U} is the eigenvector matrix for $\hat{\mathcal{D}}_{\mathbf{n}}(\pi, \epsilon)$ operator.

Appendix B: Global symmetries

The explicit matrix representations for time-reversal and particle-hole symmetry operators in BdG formalism are given by $\hat{T} = i \hat{\zeta}_0 \otimes \hat{\sigma}_x \otimes \hat{\sigma}_y \mathcal{K}$ and $\hat{\mathcal{P}} = \hat{\zeta}_x \otimes \hat{\sigma}_0 \otimes \hat{\sigma}_0 \mathcal{K}$, respectively. Here, \mathcal{K} is the complex-conjugate operator, $\hat{\zeta}_i$ and $\hat{\sigma}_i$ with $i \in \{0, x, y, z\}$ are Pauli matrices acting on particle-hole and spin subspaces, respectively. The symmetry relation reads $\hat{O} \hat{H}^*(\mathbf{k}) \hat{O}^{-1} = \epsilon \hat{H}(-\mathbf{k})$ with $\epsilon = +1(-1)$ for $\hat{O} = \hat{T}(\hat{\mathcal{P}})$. Additionally, we can construct a chiral symmetry operator $\hat{C} = \hat{T} \hat{\mathcal{P}}$ fulfilling $\hat{C} \hat{H}(\mathbf{k}) \hat{C}^{-1} = -\hat{H}(\mathbf{k})$ [83, 85, 86]. The symmetry operators have the properties $\hat{T}^2 = -1$ and $\hat{\mathcal{P}}^2 = 1$. In addition, the inversion symmetry operator is defined by $\hat{\mathcal{P}}_u = \hat{\sigma}_z \otimes \hat{P}$ fulfilling $\hat{\mathcal{P}}_u^2 = 1$.

We complete our discussion on topological phase transitions induced by FE pairing by proposing an alternative approach to calculate the topological index due to

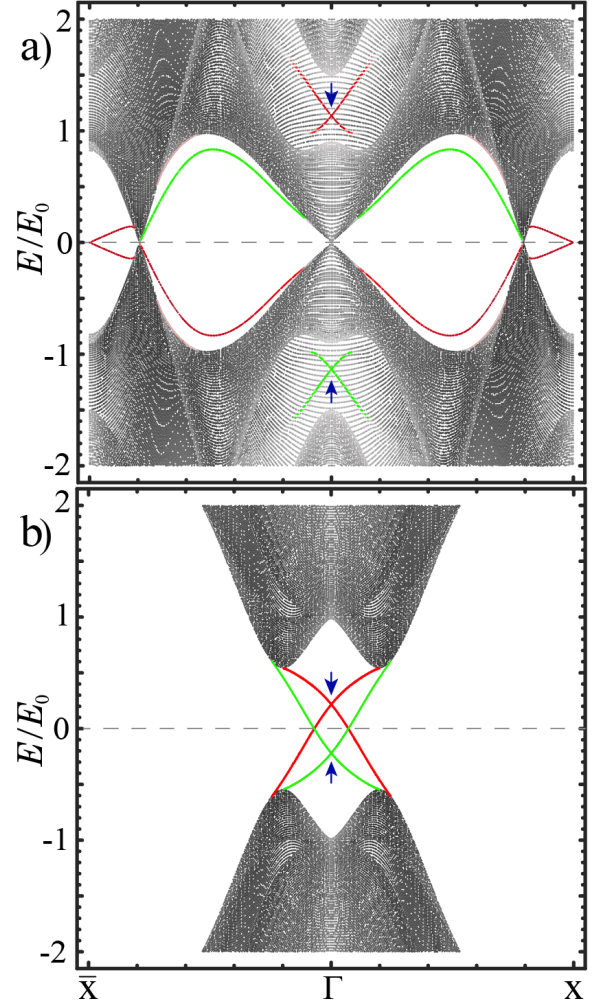


Figure 4. Enlarged view of the spectra given in Fig. 2(c) of the main text. The thickness is 180 layers and $E_0 = \Delta/2$. The high-symmetry points are $X = (0, \pi/a, 0)$ and $\Gamma = (0, 0, 0)$ where a is the lattice constant in tight binding calculations. The surface (bulk) states are colorful (dark). Blue arrows indicate the helical Dirac points induced by topological FE pairing. The gray dashed line indicates the Fermi energy. (a) [(b)] Surface states inside (outside) of the bulk states before (after) a Lifshitz transition for $\mu = -5.2E_0$ ($\mu = -E_0$). (b) The helical surface states resemble a butterfly shape, and establish dispersive Majorana modes away from the high symmetry points at the Fermi energy. The other parameters are $\alpha = -\Delta/2$ and $\beta = 0.3\alpha$.

the presence of inversion symmetry [82, 84]. The BdG Hamiltonian commutes with $\hat{\mathcal{P}}_u$ and \hat{T} operators at eight PTRIM given by

$$\begin{aligned} \mathbf{k}_p = (0,0,0), \mathbf{k}_p = (0,0,\pi), \mathbf{k}_p = (0,\pi,0), \mathbf{k}_p = (\pi,0,0), \\ \mathbf{k}_p = (0,\pi,\pi), \mathbf{k}_p = (\pi,\pi,0), \mathbf{k}_p = (\pi,0,\pi), \mathbf{k}_p = (\pi,\pi,\pi). \end{aligned} \quad (\text{B1})$$

Generally, the FE pairing arising from odd-parity pairing channels can induce topological phase transition along

	$\hat{\mathcal{T}}$	$\hat{\mathcal{P}}$	$\hat{\mathcal{C}}$	$\hat{\mathcal{P}}_u$
$\hat{\mathcal{T}}$	Commute	Commute	Commute	Commute
$\hat{\mathcal{P}}$		Commute	Commute	Anticommute
$\hat{\mathcal{C}}$			Commute	Anticommute
$\hat{\mathcal{P}}_u$				Commute

Table II. Commutation/anticommutation relations between the discrete symmetries.

the directions \mathbf{K} connecting the PTRIM. The criteria rely on the presence and absence of finite and low energy pairings along such directions, respectively. In this case, the BdG Hamiltonian becomes block diagonal

$$\hat{\mathcal{H}}'(\mathbf{K}) = \text{diag}(\hat{h}_{\mathbf{K},+}^{+-}, \hat{h}_{\mathbf{K},+}^{+-}, \hat{h}_{\mathbf{K},-}^{-+}, \hat{h}_{\mathbf{K},-}^{-+}), \quad (\text{B2})$$

where

$$\hat{h}_{\mathbf{K},\lambda}^{+-} = \begin{pmatrix} -E_{\mathbf{K}}^- & (\delta_{\mathbf{K},\lambda}^{+-})^* \\ \delta_{\mathbf{K},\lambda}^{+-} & E_{\mathbf{K}}^+ \end{pmatrix}. \quad (\text{B3})$$

In Eq. (B2), $\hat{h}_{\mathbf{K},\lambda}^{-+}$ is the particle-hole partner of $\hat{h}_{\mathbf{K},\lambda}^{+-}$ implied by $\hat{\tau}_y(\hat{h}_{\mathbf{K},\lambda}^{+-})^*\hat{\tau}_y^{-1} = \hat{h}_{\mathbf{K},\lambda}^{-+}$. Note that each block $\hat{h}_{\mathbf{K},\lambda}^{\pm\mp}$ preserves an effective time-reversal symmetry $\hat{T} = \mathcal{K}$ with $\hat{T}^2 = +1$. Particle-hole symmetry and the conventional time-reversal symmetry with $\hat{T}^2 = -1$ are broken due to the different diagonal entries in the symmetry blocks. Also, each block in Eq. (B2) satisfies inversion symmetry implied by $\hat{\tau}_z\hat{h}_{\mathbf{K},\lambda}^{\nu\nu'}\hat{\tau}_z^{-1} = \hat{h}_{-\mathbf{K},\lambda}^{\nu\nu'}$ with $\nu, \nu' \in \{+, -\}$. In this case, $\hat{h}_{\mathbf{K},\lambda}^{\nu\nu'}$ commutes with $\hat{\tau}_z$, and the negative parity of the eigenstates associated to the lower energy band in sector $\hat{h}_{\mathbf{K},\lambda}^{\nu\nu'}$ determines the topological nature of the phase transition. Note that only one of the directions connecting the PTRIM is sufficient to capture the nontrivial topological phase induced by FE Cooper pairing. Therefore, to characterize the topological phases, we define a topological index

$$\mathcal{N} = |n_{\Gamma} - n_{\mathbf{p}}|, \quad (\text{B4})$$

where n_{Γ} and $n_{\mathbf{p}}$ are the number of negative eigenvalues of the parity operator at the Γ point $\mathbf{k}_{\mathbf{p}} = (0,0,0)$, and other PTRIM. Note that \mathcal{N} is a \mathbb{Z}_2 topological index taking two values, i.e., $\mathcal{N} = 1(0)$ in the topologically nontrivial (trivial) phase. The full topological index can be derived by the summation of the topological indices associated to the decoupled blocks in Eq. (B2) as

$$Z = \sum_{\lambda=\pm} (\mathcal{N}_{\lambda}^{+-} + \mathcal{N}_{\lambda}^{-+}), \quad (\text{B5})$$

where $\mathcal{N}_{\lambda}^{\nu\nu'}$ corresponds to the block $\hat{h}_{\mathbf{K},\lambda}^{\nu\nu'}$. In the topologically nontrivial phase, conservation of parity leads to the quantization of the topological index and the

emergence of surface states. Pseudospin rotation symmetry ensures that the surface states come in pairs establishing FE helical Dirac points. Hence, the appearance of a pair of helical surface states at positive (negative) excitation energies is signaled by $\sum_{\lambda=\pm} \mathcal{N}_{\lambda}^{+-} = 2$ ($\sum_{\lambda=\pm} \mathcal{N}_{\lambda}^{-+} = 2$). Considering two surfaces, we observe four Dirac surface states on each surface (two for positive excitation energies and two for negative energies) due to parity-time-reversal symmetry, cf. Fig. 3.

A Lifshitz transition can move the FE helical Dirac surface states, shown in Fig. 4(a), to the low energies. In this case, the surface states establish Majorana modes at the Fermi energy, see Fig. 4(b).

Note that the point group symmetry of the normal-state Hamiltonian for any real system is lower than the $O(3)$ symmetry of the Luttinger-Kohn Hamiltonian discussed in the main text. The Luttinger-Kohn Hamiltonian serves as a valuable approximation for energy bands close to high-symmetry points. However, the symmetry of the superconducting (BdG) Hamiltonian is relevant for our analysis. It belongs to the O_h symmetry group, as the $O(3)$ symmetry of the normal state transforms into cubic point group symmetry due to the pairing matrices derived through irreducible representations of the cubic point group symmetry. Importantly, the pseudospin rotation symmetry mentioned above is present for multi-band system with parity-time-reversal symmetry. Its presence is independent of the $O(3)$ symmetry of the normal state Hamiltonian. Nonetheless, we examine our predictions when the normal state is influenced by $O(3)$ symmetry-breaking terms. To this end, we incorporate the cubic spin-orbit coupling term to the normal state Hamiltonian as

$$\hat{\mathcal{H}}(\mathbf{k}) = \alpha|\mathbf{k}|^2\hat{I}_4 + \beta \sum_i k_i^2 \hat{J}_i^2 + \gamma \sum_{i \neq j} k_i k_j \hat{J}_i \hat{J}_j - \mu, \quad (\text{B6})$$

where γ parametrizes the strength of the cubic spin-orbit coupling term. This Hamiltonian refers to the $O(3)$ symmetry-broken case in the normal state if $\gamma \neq \beta$. We adopt the tight-binding regularization of Eq. (B6) in the BdG form. The spectral result within the topologically non-trivial phase is illustrated in Fig. 5. Evidently, we can also observe the emergence of helical Dirac surface states with particle-hole character away from the Fermi energy due to the unconventional finite energy Cooper pairing in the case with broken $O(3)$ symmetry, see Fig. 5(a,b). In addition, we investigate a Lifshitz transition around the Γ point by a variation of the chemical potential as illustrated in Fig. 5(c,d). In this case, the surface states are shifted towards low energies. If the superconducting gap possesses nodes at zero excitation energy, these surface states connect the nodal points, see Fig. 5(c). If the superconducting gap is fully developed at zero excitation energy, these surface states connect to the bulk states at finite excitation energy, see Fig. 5(d).

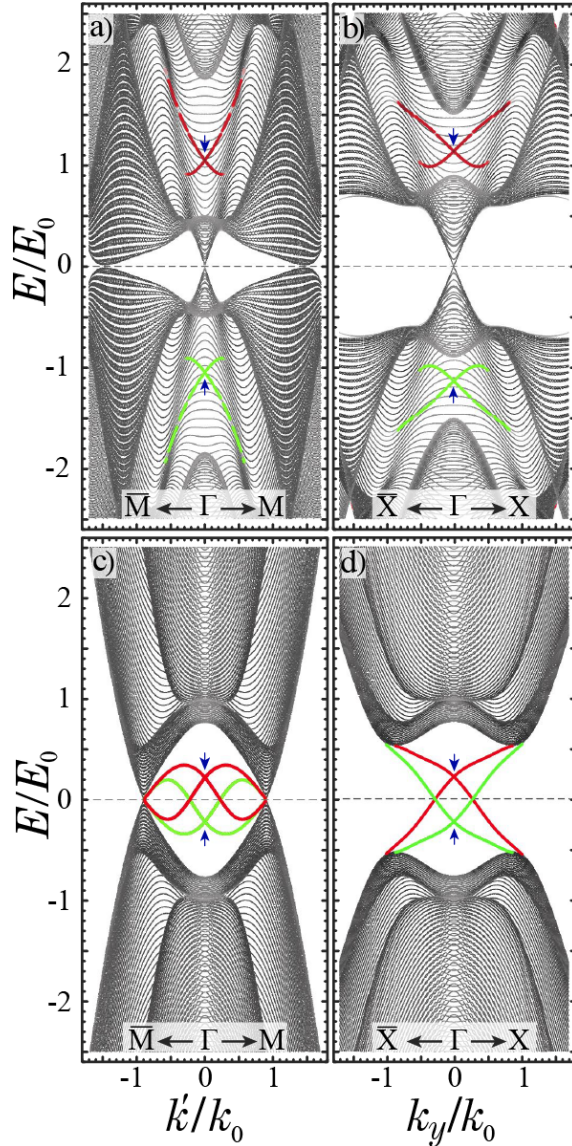


Figure 5. Spectra of a slab with (001) surfaces in the topologically nontrivial regime. The thickness is 100 layers. The cubic spin-orbit coupling term is chosen as $\gamma = \alpha$. Hence, $O(3)$ symmetry is broken in the normal state. In panels (a) and (c), k' defines the direction in momentum space with $k_x = k_y$. The chemical potential is chosen as (a) $\mu = -5.2E_0$, (b) $\mu = -5.1E_0$, and (c,d) $\mu = -E_0$. The other parameters are $\beta = 0.3\alpha$, $\alpha = -(2/3)\Delta$, and $E_0 = (2/3)\Delta$. The high-symmetry points are $X = (0, \pi/a, 0)$ and $M = (\pi/a, \pi/a, 0)$.

Appendix C: Point group symmetry analysis

The block diagonalization of the BdG Hamiltonian is possible in directions where the pairing potential satisfies two conditions:

1. vanishing intraband pairing,
2. nonvanishing interband pairing at finite energies.

These two conditions can be fulfilled when time-reversal

T symmetry combines with twofold rotation about the $\langle 110 \rangle$ axis. This symmetry operator is defined by $\hat{C}_T \equiv \hat{T}\hat{C}_{2,x+y}$ having the property $\hat{C}_T^2 = 1$. We then use the $\hat{C}_{2,x+y}$ operator combined with inversion \hat{P} symmetry (mirror reflection), denoted as $\hat{C}_P \equiv \hat{P}\hat{C}_{2,x+y}$, for block diagonalization. In addition, the double degeneracy of states at each momenta is ensured by $\hat{P}\hat{T} = e^{-i\pi}\hat{C}_T\hat{C}_P$. Note that \hat{T} , $\hat{C}_{2,x+y}$, and \hat{P} commute with each other, and $\hat{C}_P^2 = -1$.

In the following, we illustrate these points by group theoretical analysis. We begin by analyzing the point group symmetry of the given BdG Hamiltonian

$$\hat{H}_{\text{BdG}}(\mathbf{k}) = \begin{pmatrix} \hat{H}(\mathbf{k}) & \hat{\Delta}(\mathbf{k}) \\ \hat{\Delta}^\dagger(\mathbf{k}) & -\hat{H}^T(-\mathbf{k}) \end{pmatrix} \quad (\text{C1})$$

where $\hat{H}(\mathbf{k})$ and $\hat{\Delta}(\mathbf{k}) = \hat{D}(\mathbf{k})e^{i\pi\hat{J}_y}$ denote normal state and pairing matrix, respectively. $\hat{H}_{\text{BdG}}(\mathbf{k})$ preserves the symmetry group G if its symmetry elements, denoted as \hat{g} , satisfy the following condition

$$\hat{H}(\mathbf{k}) \mapsto \hat{g}\hat{H}(R^{-1}\mathbf{k})\hat{g}^\dagger, \quad \hat{D}(\mathbf{k}) \mapsto \hat{g}\hat{D}(R^{-1}\mathbf{k})\hat{g}^\dagger, \quad (\text{C2})$$

where \hat{g} can for instance be a q -fold rotation and R is a 3×3 orthogonal matrix implementing rotation on momentum space. Then, the point group symmetry operation for Eq. (C1) takes the form

$$\hat{G}\hat{H}_{\text{BdG}}(R^{-1}\mathbf{k})\hat{G}^{-1} = \hat{H}_{\text{BdG}}(\mathbf{k}), \quad (\text{C3})$$

where $\hat{G} = \text{diag}(\hat{g}, \pm\hat{g}^*)$. In our system, G for the superconducting Hamiltonian is given by

$$G = U(1) \otimes \mathcal{P} \otimes T \otimes O_h, \quad (\text{C4})$$

where $U(1)$ is a global phase-rotation symmetry, \mathcal{P} (T) denotes anti-unitary particle-hole (time-reversal) symmetry, and O_h is a cubic point group symmetry. O_h describes the combination of inversion symmetry P and octahedral O point group symmetry. The O group consists of q -fold rotations about the \mathbf{n} axis labeled by $C_{q,\mathbf{n}}$. Combining P with O , this results in q -fold improper rotations denoted by $PC_{q,\mathbf{n}}$.

In our study, the pairing channels are odd (even) under \hat{P} (\hat{T}) symmetries such that $\hat{M}\hat{D}(-\mathbf{k})\hat{M}^\dagger = -(+)\hat{D}(\mathbf{k})$ with $\hat{M} = \hat{P}(\hat{T})$. Moreover, $\hat{D}(\mathbf{k})$ anti-commute with $\hat{P}\hat{T}$ symmetry, i.e., $\{\hat{D}(\mathbf{k}), \hat{P}\hat{T}\} = 0$ with $\hat{T} = \exp(i\pi\hat{J}_y)\mathcal{K}$ and $\hat{P} = \hat{I}_4$, where \mathcal{K} is complex conjugation. Importantly, the generators of $\hat{D}(\mathbf{k})$ in combination with \hat{T} symmetry, this can impose constraints on the pairing potential. In the main text, we focus on the A_{2u} pairing channel (spin-septet). The matrix representation of $\hat{D}(\mathbf{k})$ is $\hat{D}(\mathbf{k}) = \mathbf{k} \cdot \hat{\mathbf{T}}$ where $\hat{T}_i = \{\hat{J}_i, \hat{J}_{i+1}^2 - \hat{J}_{i+2}^2\}$ with $i+1 = y$ if $i = x$, etc., cyclically. The generators for the A_{2u} channel are $\{e^{i\pi}\hat{C}_{4z}, e^{i\pi}\hat{C}_{2,z+x}\}$, where $\hat{C}_{2,z+x}$ (\hat{C}_{4z}) denotes two(four)fold rotation about the $[1,0,1]$ ($[0,0,1]$) axis [63]. Note that \hat{C}_{4z} does not constrain the pairing

channel while the rotation about C'_2 axis does. In this case, normal state and pairing channel transform under twofold rotation about the C'_2 axis, e.g., $[1,1,0]$ axis, such that

$$\hat{C}_{2,x+y} \hat{D}(k_y, k_x, -k_z) \hat{C}_{2,x+y}^\dagger = -\hat{D}(\mathbf{k}), \quad (\text{C5})$$

$$\hat{C}_{2,x+y} \hat{E}(k_y, k_x, -k_z) \hat{C}_{2,x+y}^\dagger = \hat{E}(\mathbf{k}). \quad (\text{C6})$$

Combining \hat{T} with twofold rotation symmetry denoted by $\hat{C}_T = \hat{T} \hat{C}_{2,x+y}$, yielding the relation

$$\hat{C}_T \hat{D}(-k_y, -k_x, k_z) \hat{C}_T^\dagger = -\hat{D}(\mathbf{k}), \quad (\text{C7})$$

$$\hat{C}_T \hat{E}(-k_y, -k_x, k_z) \hat{C}_T^\dagger = \hat{E}(\mathbf{k}). \quad (\text{C8})$$

In this case, \hat{C}_T results in vanishing (nonvanishing) intraband (interband) pairing potentials.

We prove this at two Fermi momenta \mathbf{k}_1 and \mathbf{k}_2 (due to having two energy bands), and the crossing momenta \mathbf{k}_3 at finite energies. Note that \mathbf{k}_1 (\mathbf{k}_2) is associated to the Fermi momentum for the $|m_j| = 3/2$ ($|m_j| = 1/2$) Fermi surface. The $|m_j| = 1/2$ Fermi surface is constrained in a similar way by \hat{C}_T as the $|m_j| = 3/2$ Fermi surface. This results in point nodes in both double-degenerate Fermi surfaces along the $\langle 001 \rangle$ direction. We prove this through symmetry analysis in pseudospin (Kramer's partner) representation. The double-degeneracy is guaranteed by PT symmetry. In this case, the effective pairing projected onto the intraband basis at \mathbf{k}_1 can be represented in the pseudospin basis as

$$\hat{\Delta}_{\text{eff}}^{\nu\nu}(\mathbf{k}_1) \equiv (\mathbf{d}(\mathbf{k}_1) \cdot \hat{\sigma})(i\hat{\sigma}_y), \quad (\text{C9})$$

where $\mathbf{d}(\mathbf{k}_1) = (d_x(\mathbf{k}_1), d_y(\mathbf{k}_1), d_z(\mathbf{k}_1))$, $\hat{\sigma} = (\hat{\sigma}_x, \hat{\sigma}_y, \hat{\sigma}_z)$ is the vector of Pauli matrices in intraband pseudospin basis. Note that $\hat{\Delta}_{\text{eff}}^{\nu\nu}(\mathbf{k}_1)$ is represented in pseudospin triplet state due to the odd parity of $\hat{D}(\mathbf{k})$. For $\nu = +$, $\hat{\Delta}_{\text{eff}}^{\nu\nu}(\mathbf{k}_1)$ describes pairing of $|m_j| = 3/2$ states at the Fermi energy. At \mathbf{k}_1 , spin and momentum transform under \hat{C}_T as

$$\hat{C}_T \hat{\sigma} \hat{C}_T^\dagger = (-\hat{\sigma}_y, -\hat{\sigma}_x, \hat{\sigma}_z), \quad R^{-1} \mathbf{k}_1 = (-k_y, -k_x, k_z). \quad (\text{C10})$$

Consequently, along the $\langle 001 \rangle$ direction, the effective pairing potential becomes $\hat{\Delta}_{\text{eff}}^{++}(\mathbf{k}_1) = d_z(k_z) \hat{\sigma}_z (i\hat{\sigma}_x)$ which violates the Fermi statistics unless $d_z(k_z) = 0$. Consequently, this results in point nodes along z -direction (and all equivalent directions). Moreover, the same holds true for $\hat{\Delta}_{\text{eff}}^{--}(\mathbf{k}_2)$. Therefore, point 1., stated at the beginning of this section, is fulfilled leading to

$$\hat{\Delta}_{\text{eff}}^{++}(\mathbf{k}_1) = \hat{\Delta}_{\text{eff}}^{--}(\mathbf{k}_2) = 0. \quad (\text{C11})$$

To realize point 2., stated at the beginning of this section, we analyze how interband pairing is affected by \hat{C}_T symmetry. Finite energy pairing happens at interband momenta \mathbf{k}_3 where double-degenerate $|m_j| = 3/2$ electron states cross with $|m_j| = 1/2$ hole bands away from

the Fermi energy. We can expand the interband pairing matrix $\hat{\Delta}_{\text{eff}}^{+-}(\mathbf{k}_3)$ as

$$\hat{\Delta}_{\text{eff}}^{+-}(\mathbf{k}_3) = \mathbf{g}_{\mathbf{k}_3}^{+-} \cdot \hat{\tau}, \quad (\text{C12})$$

where $\mathbf{g}_{\mathbf{k}_3}^{+-}$ is a four component vector given by

$$\mathbf{g}_{\mathbf{k}_3}^{+-} = (\mathbf{g}_{0,\mathbf{k}_3}^{+-}, \mathbf{g}_{x,\mathbf{k}_3}^{+-}, \mathbf{g}_{y,\mathbf{k}_3}^{+-}, \mathbf{g}_{z,\mathbf{k}_3}^{+-}), \quad (\text{C13})$$

and $\hat{\tau} = (\hat{\tau}_0, \hat{\tau}_x, \hat{\tau}_y, \hat{\tau}_z)$ being the four component vector of Pauli matrices represented in interband pseudospin basis. Applying \hat{C}_T symmetry on $\hat{\tau}$ produce the same results as mentioned in Eq. (C10) for $\hat{\sigma}$. In this case, $\hat{\tau}_0$ and $\hat{\tau}_z$ remain invariant along the $\langle 001 \rangle$ direction. Consequently, the interband pairing matrix becomes

$$\hat{\Delta}_{\text{eff}}^{+-}(k_z) = \mathbf{g}_{0,k_z}^{+-} \hat{\tau}_0 + \mathbf{g}_{z,k_z}^{+-} \hat{\tau}_z. \quad (\text{C14})$$

It is worth mentioning that $\hat{\tau}_0$ is allowed by the Pauli exclusion principle if we exchange band indices in addition to spin indices. Importantly, $\hat{\Delta}_{\text{eff}}^{+-}(k_z)$ is constrained by \hat{C}_T such that only up to two components of the $\mathbf{g}_{\mathbf{k}_2}^{+-}$ vector are finite. This is identical with our analysis based on rotational symmetry in pseudospin basis described in Sec. A. The $\hat{\tau}_z$ remains invariant under two-fold rotation in pseudospin space combined with time-reversal symmetry.

Despite our pairing model is odd in parity, we can define an inversion operator in BdG form as

$$\hat{G} = \text{diag}(\hat{I}_4, -\hat{I}_4) = \hat{\sigma}_z \otimes \hat{I}_4 \quad (\text{C15})$$

where

$$\hat{G} \hat{H}_{\text{BdG}}(-\mathbf{k}) \hat{G}^{-1} = \hat{H}_{\text{BdG}}(\mathbf{k}). \quad (\text{C16})$$

In this case, the results given in Eqs. (C11) and (C14) hold true for \hat{C}_P .

Importantly, such symmetries enforce the BdG Hamiltonian to become block diagonal along the topological phase transition directions and at finite excitation energies. This is a direct consequence of Eqs. (C11) and (C14). Although \hat{C}_T is anti-unitary, the twofold degeneracy can be lifted in the eigenspace of mirror reflection symmetry as

$$\hat{Y}^{-1} \hat{H}_{\text{BdG}}(k_z) \hat{Y} = \text{diag}(\hat{H}_{+i}(k_z), \hat{H}_{-i}(k_z)), \quad (\text{C17})$$

where \hat{Y} is the matrix of eigenvectors for \hat{C}_P operator, and $\hat{H}_\lambda(\mathbf{k})$ is a 4×4 block labeled with eigenvalues of $\hat{P} \hat{C}_{2,x+y}$ as $\lambda = \pm i$. Note that $\hat{H}_{+i}(k_z) = \hat{H}_{-i}(k_z)$ with

$$\hat{H}_{+i}(k_z) = \begin{pmatrix} -E_{k_z}^+ & 0 & 0 & \Delta k_z \\ 0 & -E_{k_z}^- & \Delta k_z & 0 \\ 0 & \Delta k_z & E_{k_z}^+ & 0 \\ \Delta k_z & 0 & 0 & E_{k_z}^- \end{pmatrix}, \quad (\text{C18})$$

where $\Delta = (\sqrt{3}/2)\Delta$. The pairing sector is situated on the off-diagonal block of $\hat{H}_{\pm i}(\mathbf{k})$ with vanishing intra-band pairing. $\hat{H}_{\pm i}(\mathbf{k})$ can be further brought into block diagonal form through the transformation \hat{W} onto the interband basis. Such a transformation is given by

$$\begin{aligned}\hat{\mathcal{H}}'(k_z) &= \hat{W}^{-1} \left(\hat{Y}^{-1} \hat{H}_{\text{BdG}}(k_z) \hat{Y} \right) \hat{W} \\ &= \text{diag} \left(\hat{h}_{k_z, +i}^{-+}, \hat{h}_{k_z, +i}^{+-}, \hat{h}_{k_z, -i}^{-+}, \hat{h}_{k_z, -i}^{+-} \right),\end{aligned}\quad (\text{C19})$$

where

$$\hat{h}_{k_z, \lambda}^{\nu\nu'} = \begin{pmatrix} -E_{k_z}^{\nu\nu'} & \Delta k_z \\ \Delta k_z & E_{k_z}^{\nu\nu'} \end{pmatrix},\quad (\text{C20})$$

and

$$\hat{W} = \begin{pmatrix} 1 & 0 & 0 & 0 & 0 & 0 & 0 & 0 \\ 0 & 0 & 1 & 0 & 0 & 0 & 0 & 0 \\ 0 & 0 & 0 & 1 & 0 & 0 & 0 & 0 \\ 0 & 1 & 0 & 0 & 0 & 0 & 0 & 0 \\ 0 & 0 & 0 & 0 & 1 & 0 & 0 & 0 \\ 0 & 0 & 0 & 0 & 0 & 0 & 1 & 0 \\ 0 & 0 & 0 & 0 & 0 & 0 & 0 & 1 \\ 0 & 0 & 0 & 0 & 0 & 1 & 0 & 0 \end{pmatrix}.\quad (\text{C21})$$

Notably, Eq. (C19) is identical to Eq. (6) of the main text. The effective Hamiltonian $\hat{\mathbb{H}}(k_x, k_y)$ for the helical surface states at finite excitation energies (see Eq. (8) of the main text) fulfills the symmetry relation

$$\hat{C}_T \hat{\mathbb{H}}(k_x, k_y) \hat{C}_T^{-1} = \hat{C}_P \hat{\mathbb{H}}(k_x, k_y) \hat{C}_P^{-1} = \hat{\mathbb{H}}(-k_y, -k_x).\quad (\text{C22})$$

Appendix D: Stability of helical Dirac surface states at finite energies

To investigate the stability of helical topological surface states at finite excitation energies, we add randomness to chemical potential and magnetization of each layer in z -direction by

$$H_R(\mathbf{k}_{\parallel}, z) = \sum_{n_z} \sum_{\mathbf{k}_{\parallel}} \hat{\psi}_{\mathbf{k}_{\parallel}, z}^{\dagger} \left(\mu_{n_z} + \mathbf{M}_{n_z} \cdot \hat{\mathbf{J}} \right) \hat{\psi}_{\mathbf{k}_{\parallel}, z},\quad (\text{D1})$$

where the basis in $j = 3/2$ representation is

$$\hat{\psi}_{\mathbf{k}_{\parallel}, z}^{\dagger} = \left(c_{\frac{3}{2}, \mathbf{k}_{\parallel}, z}^{\dagger}, c_{\frac{1}{2}, \mathbf{k}_{\parallel}, z}^{\dagger}, c_{-\frac{1}{2}, \mathbf{k}_{\parallel}, z}^{\dagger}, c_{-\frac{3}{2}, \mathbf{k}_{\parallel}, z}^{\dagger} \right).\quad (\text{D2})$$

In Eq. (D1), we consider k_z to be no longer conserved. Instead, $n_z = 0, \dots, N_z$ is the layer index with N_z the total number of layers along the z -axis; $\sum_{\mathbf{k}_{\parallel}} = \sum_{k_x} \sum_{k_y}$, $\mathbf{k}_{\parallel} = (k_x, k_y)$ represents the conserved momenta; $\hat{\mathbf{J}} = (\hat{J}_x, \hat{J}_y, \hat{J}_z)$ is the vector of angular momenta; μ_{n_i} denotes the nonmagnetic onsite potential at layer n_i where

the strength is a uniformly distributed random number within the interval $\mu_{n_i} \in [0, \Delta]$; the Zeeman field vector is $\mathbf{M}_{n_i} = (M_{x, n_i}, M_{y, n_i}, 0)$, with the strength $M_{x(y), n_i}$, taken as uniformly distributed random number in the interval $M_{x(y), n_i} \in [0, 0.06\Delta]$. The numerical results are shown in Fig. 6(a1-a3) and 6(b1-b3). We can observe in Fig. 6(a1) and (a2) that bulk and surface states become broadened while the topological surface states remain intact in the presence of nonmagnetic randomness at finite excitation energies since \hat{C}_T symmetry is preserved. When the system is subjected to magnetic randomness, the degeneracy of surface states are lifted due to broken time-reversal symmetry. In this case, \hat{C}_T is broken. Along k_y direction (see Fig. 6(b2) and 6(b3)), the Dirac cone is gapped.

Furthermore, the symmetry \hat{P} can be broken by introducing $\hat{H}_{\delta}(\mathbf{k})$ to Eq. (B6), where $H_{\delta}(\mathbf{k})$ is defined as

$$\hat{H}_{\delta}(\mathbf{k}) = \delta \sum_i k_i \left(\hat{J}_{i+1} \hat{J}_i \hat{J}_{i+1} - \hat{J}_{i+2} \hat{J}_i \hat{J}_{i+2} \right),\quad (\text{D3})$$

with δ denoting the strength of anti-symmetric spin-orbit coupling (ASOC). This term originates from T_d point group symmetry. Note that both $\hat{C}_{2, x+y}$ and \hat{P} symmetries are absent in $\hat{H}_{\delta}(\mathbf{k})$ since

$$\hat{C}_{2, x+y} \hat{H}_{\delta}(\mathbf{k}) \hat{C}_{2, x+y}^{\dagger} \neq \hat{H}_{\delta}(k_y, k_x, -k_z),\quad (\text{D4})$$

$$\hat{P} \hat{H}_{\delta}(\mathbf{k}) \hat{P}^{\dagger} \neq \hat{H}_{\delta}(\mathbf{k}).\quad (\text{D5})$$

Consequently, \hat{C}_T is broken due to absence of $\hat{C}_{2, x+y}$ symmetry. In this case, the low-energy superconducting nodes are lifted along the TPT directions for a sufficiently large δ (of the same order of symmetric spin-orbit coupling), and the topological surface states become unstable. To illustrate this, the excitation spectra are plotted in Figs. 6 (c1-c3) in the presence of $H_{\delta}(\mathbf{k})$. Clearly, the surface states emerging from the finite energy gap closing point hybridize with the bulk states at large momentum. This can be understood from Eq. (6) since then the block diagonalization is no applicable.

This analysis identifies \hat{C}_T symmetry is required for the stability of the surface states.

Appendix E: Helical Dirac surface states at finite energies

In this section, we provide details for the derivation of the helical Dirac surface states described in the main text. The BdG Hamiltonian along the [001] direction becomes

$$\hat{H}(k_z) = \begin{pmatrix} \hat{H}_1 & 0 & \hat{H}_3 & 0 \\ 0 & \hat{H}_2 & 0 & \hat{H}_3 \\ \hat{H}_3 & 0 & -\hat{H}_1 & 0 \\ 0 & \hat{H}_3 & 0 & -\hat{H}_2 \end{pmatrix},\quad (\text{E1})$$

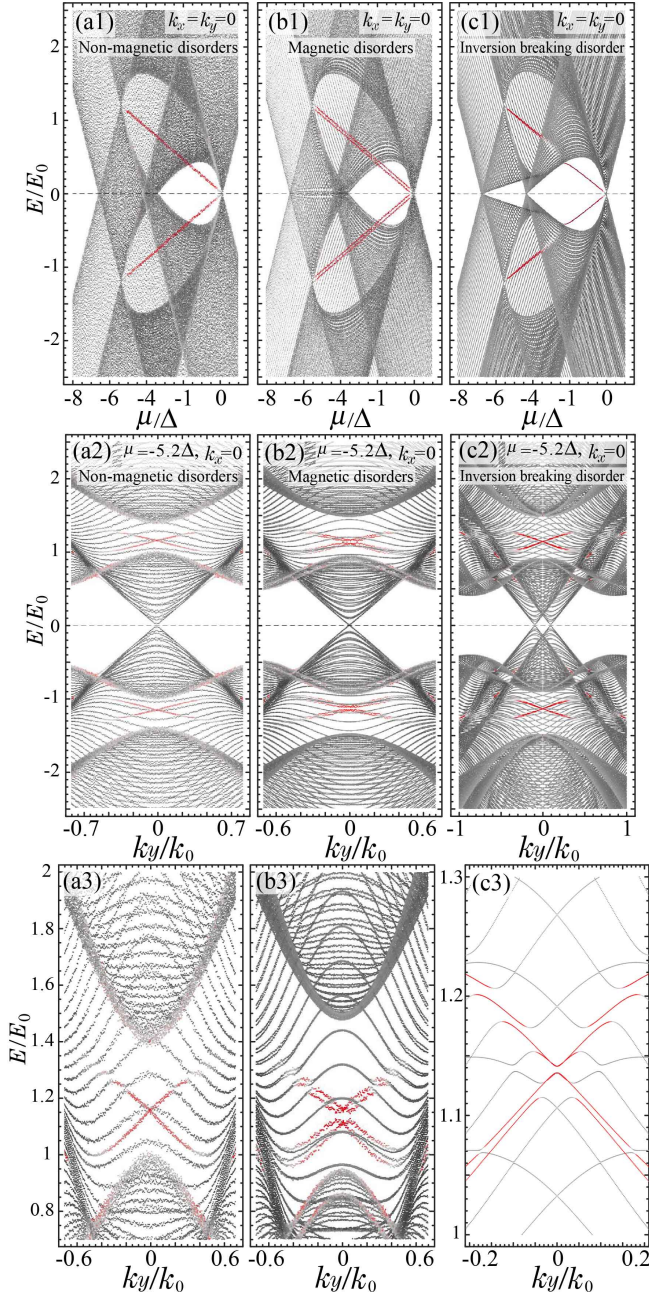


Figure 6. Excitation spectrum for (001) slab in the presence of nonmagnetic randomness with strength (a1) $v_i \in \{0, \Delta\}$ for 120 layers, (a2,a3) $v_i \in \{0, 0.6\Delta\}$ for 80 layers, (b2-b3) magnetic randomness with the form $M_{x,n_i} \hat{J}_x + M_{y,n_i} \hat{J}_y$ with $M_{x(y),n_i} \in \{0, 0.2\Delta\}$ for 80 layers (c1-c3) inversion symmetry breaking spin-orbit coupling $\delta = 0.3\Delta$ for 120 layers. Panels (a3), (b3) and (c3) are the enlarged view of the top panels. Other parameters are $(\alpha, \beta, \gamma, \mu) = -(1, 0.3, 1, 5.2)\Delta$. Note that $\gamma \neq \beta$ indicates broken $O(3)$ symmetry in the normal state. The extended bulk (surface) states are illustrated by gray (red) color according to inverse participation ratio.

with

$$\hat{H}_1 = \text{diag}(E_{k_z}^+, E_{k_z}^-), \quad \hat{H}_2 = \text{diag}(E_{k_z}^-, E_{k_z}^+), \quad (\text{E2})$$

where $E_{k_z}^+ = (\alpha + 9\beta/4)k_z^2 - \mu$, $E_{k_z}^- = (\alpha + \beta/4)k_z^2 - \mu$, $\hat{H}_3 = \Delta k_z \hat{\sigma}_x$, and $\Delta = \sqrt{3}\Delta/2$. To be able to apply our theory, presented in Eqs. (2-6) of the main text, we should represent $\hat{H}(k_z)$ in the pseudospin basis where each diagonal block contains a pair of doubly degenerate bands. This can be done through the unitary transformation $\hat{\mathcal{U}}_1$

$$\hat{H}_1(k_z) = \hat{\mathcal{U}}_1^\dagger H(k_z) \hat{\mathcal{U}}_1 \quad (\text{E3})$$

$$= \begin{pmatrix} E_{k_z}^+ & 0 & 0 & \Delta k_z \\ 0 & E_{k_z}^- & \Delta k_z & 0 \\ 0 & \Delta k_z & -E_{k_z}^+ & 0 \\ \Delta k_z & 0 & 0 & -E_{k_z}^- \end{pmatrix} \otimes \hat{\sigma}_0, \quad (\text{E4})$$

where the unitary matrix $\hat{\mathcal{U}}_1^\dagger = \hat{\mathcal{U}}_1^{-1}$ is given by

$$\hat{\mathcal{U}}_1 = \begin{pmatrix} 1 & 0 & 0 & 0 & 0 & 0 & 0 & 0 \\ 0 & 0 & 1 & 0 & 0 & 0 & 0 & 0 \\ 0 & 0 & 0 & 1 & 0 & 0 & 0 & 0 \\ 0 & 1 & 0 & 0 & 0 & 0 & 0 & 0 \\ 0 & 0 & 0 & 0 & 1 & 0 & 0 & 0 \\ 0 & 0 & 0 & 0 & 0 & 0 & 1 & 0 \\ 0 & 0 & 0 & 0 & 0 & 0 & 0 & 1 \\ 0 & 0 & 0 & 0 & 0 & 1 & 0 & 0 \end{pmatrix}. \quad (\text{E5})$$

In the next step, Eq. (E4) should be represented in the interband basis. This can be done through another unitary transformation $\hat{\mathcal{U}}_2$ as

$$\hat{\mathcal{H}}(k_z) = \hat{\mathcal{U}}_2^\dagger \hat{H}_1(k_z) \hat{\mathcal{U}}_2 = (\hat{\mathcal{U}}_1 \hat{\mathcal{U}}_2)^\dagger H(k_z) \hat{\mathcal{U}}_1 \hat{\mathcal{U}}_2 \quad (\text{E6})$$

$$= \begin{pmatrix} \hat{H}_{k_z}^{+-} & 0 \\ 0 & \hat{H}_{k_z}^{-+} \end{pmatrix}, \quad (\text{E7})$$

where

$$\hat{H}_{k_z}^{+-} = \begin{pmatrix} E_{k_z}^+ & \Delta k_z \\ \Delta k_z & -E_{k_z}^- \end{pmatrix} \otimes \hat{\sigma}_0, \quad (\text{E8})$$

$$\hat{H}_{k_z}^{-+} = \begin{pmatrix} E_{k_z}^- & \Delta k_z \\ \Delta k_z & -E_{k_z}^+ \end{pmatrix} \otimes \hat{\sigma}_0. \quad (\text{E9})$$

The transformation $\hat{\mathcal{U}}_2$ fulfills the unitary property $\hat{\mathcal{U}}_2^\dagger = \hat{\mathcal{U}}_2^{-1}$. Its explicit matrix form is given by

$$\hat{\mathcal{U}}_2 = \begin{pmatrix} 0 & 1 & 0 & 0 & 0 & 0 & 0 & 0 \\ 1 & 0 & 0 & 0 & 0 & 0 & 0 & 0 \\ 0 & 0 & 0 & 0 & 0 & 1 & 0 & 0 \\ 0 & 0 & 0 & 0 & 1 & 0 & 0 & 0 \\ 0 & 0 & 0 & 0 & 0 & 0 & 0 & 1 \\ 0 & 0 & 0 & 0 & 0 & 0 & 1 & 0 \\ 0 & 0 & 0 & 1 & 0 & 0 & 0 & 0 \\ 0 & 0 & 1 & 0 & 0 & 0 & 0 & 0 \end{pmatrix}. \quad (\text{E10})$$

Note that $\hat{\mathcal{H}}(k_z)$, given in Eq. (E7), is identical to Eq. (2) of the main text. In this case, $\Delta k_z \hat{\sigma}_0$ is the FE pairing potential in Eqs. (E8) and Eqs. (E9). The zeros on the off-diagonal blocks of Eq. (E7) indicate vanishing intraband pairing giving rise to the presence of nodes at the Fermi energy. The diagonal blocks in $\hat{\mathcal{H}}(k_z)$ exhibit pseudospin- π rotation symmetry along the z (x)-axis, i.e., the symmetry relations given in Eqs. (A6) and (A8). The explicit matrix form for such an operator can be obtained as

$$\hat{\mathcal{D}}_{\mathbf{n}_z}(\pi, -1) = \begin{pmatrix} 0 & i & 0 & 0 \\ i & 0 & 0 & 0 \\ 0 & 0 & 0 & i \\ 0 & 0 & i & 0 \end{pmatrix}.$$

Thus, Eq. (E7) is further reducible in the eigenspace of $\hat{\mathcal{D}}_{\mathbf{n}_z}(\pi, -1)$. This can be done through the unitary matrix $\hat{\mathcal{U}}_3$

$$\hat{\mathcal{H}}'(k_z) = \hat{\mathcal{U}}_3^\dagger \hat{\mathcal{H}}(k_z) \hat{\mathcal{U}}_3 \quad (\text{E11})$$

$$= (\hat{\mathcal{U}}_1 \hat{\mathcal{U}}_2 \hat{\mathcal{U}}_3)^\dagger H(k_z) \hat{\mathcal{U}}_1 \hat{\mathcal{U}}_2 \hat{\mathcal{U}}_3 \quad (\text{E12})$$

$$= \text{diag}(\hat{h}_{k_z, +}^{+-}, \hat{h}_{k_z, +}^{-+}, \hat{h}_{k_z, -}^{+-}, \hat{h}_{k_z, -}^{-+}), \quad (\text{E13})$$

with

$$\hat{h}_{k_z, \pm}^{+-} = \begin{pmatrix} -E_{k_z}^- & \Delta k_z \\ \Delta k_z & E_{k_z}^+ \end{pmatrix}, \quad \hat{h}_{k_z, \pm}^{-+} = \begin{pmatrix} -E_{k_z}^+ & \Delta k_z \\ \Delta k_z & E_{k_z}^- \end{pmatrix}, \quad (\text{E14})$$

and $\hat{\mathcal{U}}_3 = \text{diag}(\hat{\mathcal{V}}, \hat{\mathcal{V}})$ where $\hat{\mathcal{V}}$ is the matrix of eigenvectors of $\hat{\mathcal{D}}_{\mathbf{n}_z}(\pi, -1)$ given by

$$\hat{\mathcal{V}} = \frac{1}{\sqrt{2}} \begin{pmatrix} 0 & 1 & 0 & -1 \\ 0 & 1 & 0 & 1 \\ 1 & 0 & -1 & 0 \\ 1 & 0 & 1 & 0 \end{pmatrix}.$$

We solve the eigenvalue problem for one of the decoupled subblocks in Eq. (E13). This problem is given by $\hat{h}_{k_z, \pm}^{+-} \hat{\Phi}(\xi, z) = \mathcal{E}_{\text{DP}} \hat{\Phi}(\xi, z)$ where $\hat{\Phi}(\xi, z) = (u, v)^T \exp(\xi z)$ is the ansatz for the decaying eigenspinor. ξ denotes the localization factor, $|u|^2$ ($|v|^2$) is the probability weight for electron (hole) states with different magnetic quantum number $m_j = \pm 3/2$ ($m_j = \pm 1/2$). We consider a semi-infinite system in $z \geq 0$ space. Therefore, k_z is no longer conserved and we use its real space representation $k_z = k_z^\dagger = -i\partial_z$. In this case, the secular equation $(\hat{h}_{k_z, \pm}^{+-} - \mathcal{E}_{\text{DP}}) \hat{\Phi}(\xi, z) = 0$ can be evaluated by setting its determinant to zero,

$$\begin{vmatrix} m'\xi^2 + \mu - \mathcal{E}_{\text{DP}} & -i\Delta\xi \\ -i\Delta\xi & -(m\xi^2 + \mu) - \mathcal{E}_{\text{DP}} \end{vmatrix} = 0, \quad (\text{E15})$$

where $m = \alpha + \beta/4$ and $m' = \alpha + 9\beta/4$. The solution of the secular equation yields

$$\xi_{\pm} = \sqrt{\frac{1}{2mm'} \left(\Lambda \pm \sqrt{\Lambda^2 + 4mm'(\mathcal{E}_{\text{DP}}^2 - \mu^2)} \right)}, \quad (\text{E16})$$

where $\Lambda = \Delta^2 - \mathcal{E}_{\text{DP}}\vartheta^- - \mu\vartheta^+$ and $\vartheta^{\pm} = (m' \pm m)/2$. In the absence of pairing, i.e., for $\Delta = 0$, the localization length becomes purely imaginary leading to extended states. However, ξ_{\pm} obtains a real component in the topological phase induced by FE pairing. This leads to proper surface state solutions.

To specify the components of $\hat{\Phi}(\xi, z)$, we use the secular equation, and obtain

$$u \equiv u_l = -i\Delta\xi_l \rightarrow v \equiv v_l = m'\xi_l^2 + \mu - \mathcal{E}_{\text{DP}}, \quad (\text{E17})$$

$$v \equiv V_l = -i\Delta\xi_l \rightarrow u \equiv U_l = m\xi_l^2 + \mu + \mathcal{E}_{\text{DP}}. \quad (\text{E18})$$

Consequently, we have a pair of eigenspinors given by

$$\hat{\Phi}(\xi_l, z) = \begin{pmatrix} u_l \\ v_l \end{pmatrix} e^{\xi_l z}, \quad \hat{\Phi}'(\xi_l, z) = \begin{pmatrix} U_l \\ V_l \end{pmatrix} e^{\xi_l z}. \quad (\text{E19})$$

We can construct two sets of wave functions by the superposition of eigenspinors $\hat{\Phi}(\xi_l, z)$ ($\hat{\Phi}'(\xi_l, z)$),

$$\hat{\Psi}_1(z) = \sum_{l=\pm} C_l \hat{\Phi}(\xi_l, z), \quad \hat{\Psi}_2(z) = \sum_{l=\pm} Q_l \hat{\Phi}'(\xi_l, z), \quad (\text{E20})$$

where the summations run over the decay factors and the coefficients of the expansion are denoted by C_l and Q_l . To have surface state solutions, the wave functions and their first derivatives must vanish at the interface of the system and far away from the interface, i.e.,

$$\hat{\Psi}(\infty) = \hat{\Psi}'(\infty) = 0, \quad \hat{\Psi}(0) = \hat{\Psi}'(0) = 0. \quad (\text{E21})$$

Note that we assume just one interface in our analytical calculations. The boundary conditions at $z = 0$ give rise to two pairs of equations

$$C_- \begin{pmatrix} u_- \\ v_- \end{pmatrix} + C_+ \begin{pmatrix} u_+ \\ v_+ \end{pmatrix} = 0, \quad (\text{E22})$$

$$Q_- \begin{pmatrix} U_- \\ V_- \end{pmatrix} + Q_+ \begin{pmatrix} U_+ \\ V_+ \end{pmatrix} = 0. \quad (\text{E23})$$

Re-arranging Eqs. (E22) and (E23), we arrive at

$$\frac{C_-}{C_+} = -\frac{\xi_+}{\xi_-} = -\frac{m'\xi_+^2 + \mu - \mathcal{E}_{\text{DP}}}{m'\xi_-^2 + \mu - \mathcal{E}_{\text{DP}}}, \quad (\text{E24})$$

$$\frac{Q_-}{Q_+} = -\frac{\xi_+}{\xi_-} = -\frac{m\xi_+^2 + \mu + \mathcal{E}_{\text{DP}}}{m\xi_-^2 + \mu + \mathcal{E}_{\text{DP}}}. \quad (\text{E25})$$

Combining Eqs. (E24) and (E25) results in the explicit formula for the energy of the helical Dirac surface points \mathcal{E}_{DP} given in Eq. (7) of the main text.

Choosing $C_- = Q_- = \xi_+$ and $C_+ = Q_+ = -\xi_-$, this allows us to derive the general eigenfunction corresponding to \mathcal{E}_{DP} ,

$$\hat{\Psi}(z) = \mathcal{C} \xi_+ \begin{pmatrix} i\Delta\xi_- \\ m'\xi_-^2 + \mu - \mathcal{E}_{\text{DP}} \end{pmatrix} (e^{-\xi_- z} - e^{-\xi_+ z}), \quad (\text{E26})$$

where \mathcal{C} is the normalization factor

$$\mathcal{C} = \frac{1}{\sqrt{(|\kappa_1|^2 + |\kappa_2|^2)}} \frac{1}{\sqrt{\int_0^\infty dz |f(z)|^2}}. \quad (\text{E27})$$

Appendix F: Effective 2D helical surface Hamiltonian

In this section, we derive the effective Hamiltonian for the 2D helical surface states given in Eq. (8) of the main text. To do so, we need to project the bare BdG Hamiltonian onto the helical Dirac surface states basis. Note that $\hat{\Psi}(z)$ in Eq. (E26) is the eigenfunction corresponding to the subblock matrix $\hat{h}_{\mathbf{k},+}^-$, and we have defined $f(z) \equiv (e^{-\xi-z} - e^{-\xi+z})$, $\kappa_1 \equiv i\Delta\xi_+\xi_-$, and $\kappa_2 \equiv \xi_+(m'\xi_-^2 + \mu - \mathcal{E}_{\text{DP}})$. To have a proper projection basis, we also need the eigenfunction for the subblock $\hat{h}_{\mathbf{k},+}^{+-}$. It is given by $\hat{\varphi}(z) = \mathcal{C}(\kappa_3, \kappa_4)^T \gamma(z)$ where $\kappa_3 \equiv \xi_+(m\xi_-^2 + \mu + \mathcal{E}_{\text{DP}})$, $\kappa_4 \equiv -i\Delta\xi_+\xi_-$, and $\gamma(z) = -f(z)$.

$\hat{\Psi}(z)$ and $\hat{\varphi}(z)$ are 2×1 column vectors. In order to use them for the projection method, we convert them to 8×1 representation since the BdG Hamiltonian is a 8×8 matrix. This can be done through the transformation made by the 8×2 columns of the matrix $\hat{\mathcal{U}}^{-1} = \{\hat{\gamma}_1, \hat{\gamma}_2, \hat{\gamma}_3, \hat{\gamma}_4\}$. The first and forth subblock matrices in Eq. (E13) are identical corresponding to $\hat{h}_{\mathbf{k},+}^-$ and $\hat{h}_{\mathbf{k},-}^+$, respectively. Thus, they correspond to doubly degenerate helical surface states with eigenvalue \mathcal{E}_{DP} . Therefore, their 8×1 representations take the form

$$\hat{\Gamma}_1^- \equiv \hat{\gamma}_1 \hat{\Psi}(z) = \mathcal{C}f(z)(0, \kappa_2, 0, 0, \kappa_1, 0, 0, 0)^T, \quad (\text{F1})$$

$$\hat{\Gamma}_2^- \equiv \hat{\gamma}_4 \hat{\Psi}(z) = \mathcal{C}f(z)(0, 0, \kappa_2, 0, 0, 0, 0, \kappa_1)^T. \quad (\text{F2})$$

We repeat the above steps for $\hat{\varphi}(z)$ to obtain the proper basis for the sectors $\hat{h}_{\mathbf{k},+}^{+-}$ and $\hat{h}_{\mathbf{k},-}^{+-}$,

$$\hat{\Gamma}_1^+ \equiv \hat{\gamma}_2 \hat{\varphi}(z) = \mathcal{C}\gamma(z)(\kappa_4, 0, 0, 0, 0, \kappa_3, 0, 0)^T, \quad (\text{F3})$$

$$\hat{\Gamma}_2^+ \equiv \hat{\gamma}_3 \hat{\varphi}(z) = \mathcal{C}\gamma(z)(0, 0, 0, \kappa_4, 0, 0, \kappa_3, 0)^T. \quad (\text{F4})$$

We use Eqs. (F1-F4) as the proper orthonormal set of eigenfunctions to project the bulk superconducting Hamiltonian to the surface. Note that the orthonormality condition reads $\int_0^\infty dz [\hat{\mathcal{P}}^\nu]^\dagger \hat{\mathcal{P}}^\nu = \hat{\sigma}_0$ where $\hat{\mathcal{P}}^\pm = \{\hat{\Gamma}_1^\pm, \hat{\Gamma}_2^\pm\}$.

To derive the effective Hamiltonian for the 2D helical surface states, we consider the conserved wave vectors k_x and k_y in the BdG Hamiltonian to be small close to the Γ point. Then, we project $\hat{H}(k_x, k_y, -i\partial_z)$ onto the basis of the helical Dirac surface states. Thus, the effective Hamiltonian at finite excitation energies becomes

$$\begin{aligned} \hat{\mathbb{H}}(k_x, k_y) &= \int_0^\infty dz \hat{\mathcal{P}}^{\nu\dagger}(z) \hat{H}(k_x, k_y, -i\partial_z) \hat{\mathcal{P}}^\nu(z) \\ &= \begin{pmatrix} A_{1,1} & A_{1,2} \\ A_{2,1} & A_{2,2} \end{pmatrix}, \end{aligned} \quad (\text{F5})$$

where the matrix elements of $\hat{\mathbb{H}}(k_x, k_y)$ are given by

$$A_{i,j} = \int_0^\infty dz \hat{\Gamma}_i^\dagger(z) \hat{H}(k_x, k_y, -i\partial_z) \hat{\Gamma}_j(z), \quad (\text{F6})$$

with $i, j \in \{1, 2\}$. $\hat{\mathbb{H}}(k_x, k_y)$ should be Hermitian, thus, the matrix elements in Eq. (F5) must fulfill the relations

$$A_{1,1} = A_{1,1}^* = A_{2,2} = A_{2,2}^*, \quad (\text{F7})$$

$$A_{1,2} = A_{2,1}^*, \quad A_{2,1} = A_{1,2}^*. \quad (\text{F8})$$

After straightforward algebra, we arrive at the 2D effective Hamiltonian for the helical surface states given in Eq. (8) of the main text. Note that the group velocity of the helical topological Dirac surface states at finite excitation energies takes the form

$$v_2 = \frac{\sqrt{3}}{4} \frac{\Delta}{(|\kappa_1|^2 + |\kappa_2|^2)} \text{Im}[(\kappa_2 \kappa_1^* - \kappa_1 \kappa_2^*)]. \quad (\text{F9})$$

It is clear that v_2 depends on the components of the wave function with direct proportionality to the pairing strength Δ .

Appendix G: Energy scale for finite-energy Cooper pairing in weakly hole-doped YPdBi

In this section, we estimate the energy scale for finite-energy Cooper pairing in weakly hole-doped YPdBi. We obtain a range of $\Delta_E \approx 7.7 - 46.2 \mu\text{eV}$, which can be resolved in state-of-the-art scanning tunneling microscope (STM) [105]. We first refer to the normal state band structure of YPdBi calculated by density functional theory (DFT), see Fig. 7(a).

Close to the Γ point, the electronic structure hosts two branches of the Γ_8 bands curving downward in an energy window around $\approx 0.7\text{eV}$ before other bands coexists with the Γ_8 bands. This material is a non-centrosymmetric semimetal, which becomes superconductor at $T_c = 1.6 \text{ K}$ [97]. The absence of inversion symmetry results in weak ASOC, which leads to a mixed-parity superconducting state. Specifically, when the chemical potential resides in the $j = 3/2$ bands, the mixed-parity pairing state $A_{1g} + A_{2u}$ should be favorable in YPdBi due to T_d symmetry [67].

In the following, we estimate the value of finite-energy pairing in YPdBi. To this end, we employ a combination of DFT and analytical model analysis [37]. Our DFT calculations rely on the Kohn-Sham-Bogoliubov-de-Gennes (KS-BdG) method as implemented in the relativistic full-potential JuKKR code [100, 101]. The crystal structure for YPdBi is taken from the materials project [102], where we use a compressed lattice constant by 3% to clearly isolate the Γ_8 bands from the Γ_6 and Γ_7 bands [104]. We employ the local density approximation for the normal-state exchange-correlation functional [103] and include the effects of spin-orbit coupling as well as an angular momentum cutoff of $\ell_{\text{max}} = 3$ in the expansion of the basis into spherical harmonics. The Fermi level is shifted down such that μ lies in the range where only the Γ_8 bands persist, as indicated in Fig. 7(a). Note that the

J	O_h	η	$\hat{O}_\eta(\hat{J})$	$\hat{\eta}$	(L, S)	(L, S)
0	$A_{1g,u}$	$A_{1g,u}$	$\frac{1}{2}\hat{J}_4$	$\hat{A}_{1g,u} = \hat{N}_{0,0}$	(0, 0)	(1, 1)
1	T_{1u}	$T_{1u}^{(1)}$	$\frac{1}{\sqrt{5}}\hat{J}_z$	$\hat{T}_{1u}^{(1)} = \hat{N}_{1,0}$	×	(1, 1)
		$T_{1u}^{(2)}$	$\frac{1}{\sqrt{5}}\hat{J}_y$	$\hat{T}_{1u}^{(2)} = \frac{i}{\sqrt{2}}(\hat{N}_{1,-1} + \hat{N}_{1,1})$	×	(1, 1)
		$T_{1u}^{(3)}$	$\frac{1}{\sqrt{5}}\hat{J}_x$	$\hat{T}_{1u}^{(3)} = \frac{1}{\sqrt{2}}(\hat{N}_{1,-1} - \hat{N}_{1,1})$	×	(1, 1)
2	$E_{g,u}$	$E_{g,u}^{(1)}$	$\frac{1}{6}(3\hat{J}_z^2 - \hat{\mathbf{J}})$	$\hat{E}_{g,u}^{(1)} = \hat{N}_{2,0}$	(0, 2)	(1, 1), (1, 3)
		$E_{g,u}^{(2)}$	$\frac{1}{2\sqrt{3}}(\hat{J}_x^2 - \hat{J}_y^2)$	$\hat{E}_{g,u}^{(2)} = \frac{1}{\sqrt{2}}(\hat{N}_{2,-2} + \hat{N}_{2,2})$	(0, 2)	(1, 1), (1, 3)*
	$T_{2g,u}$	$T_{2g,u}^{(1)}$	$\frac{1}{\sqrt{3}}(\hat{J}_x\hat{J}_y + \hat{J}_y\hat{J}_x)$	$\hat{T}_{2g,u}^{(1)} = \frac{i}{\sqrt{2}}(\hat{N}_{2,-2} - \hat{N}_{2,2})$	(0, 2)	(1, 1), (1, 3)*
		$T_{2g,u}^{(2)}$	$\frac{1}{\sqrt{3}}(\hat{J}_z\hat{J}_x + \hat{J}_x\hat{J}_z)$	$\hat{T}_{2g,u}^{(2)} = \frac{i}{\sqrt{2}}(\hat{N}_{2,-1} - \hat{N}_{2,1})$	(0, 2)	(1, 1), (1, 3)*
		$T_{2g,u}^{(3)}$	$\frac{1}{\sqrt{3}}(\hat{J}_y\hat{J}_z + \hat{J}_z\hat{J}_y)$	$\hat{T}_{2g,u}^{(3)} = \frac{i}{\sqrt{2}}(\hat{N}_{2,-1} + \hat{N}_{2,1})$	(0, 2)	(1, 1), (1, 3)*
3	A_{2u}	A_{2u}	$\frac{1}{\sqrt{3}}(\hat{J}_x\hat{J}_y\hat{J}_z + \hat{J}_z\hat{J}_y\hat{J}_x)$	$\hat{A}_{2u} = \frac{i}{\sqrt{2}}(\hat{N}_{2,-2} - \hat{N}_{2,2})$	×	(1, 3)*
	T_{1u}	$T_{1u}^{(1)}$	$\frac{4}{\sqrt{365}}\hat{J}_z^3$	$\hat{T}_{1u}^{(1)} = \frac{12}{5\sqrt{73}}\hat{N}_{3,0}$	×	(1, 3)
		$T_{1u}^{(2)}$	$\frac{4}{\sqrt{365}}\hat{J}_y^3$	$\hat{T}_{1u}^{(2)} = \frac{3}{5\sqrt{73i}}[\sqrt{5}(\hat{N}_{3,-3} + \hat{N}_{3,3}) + \sqrt{3}(\hat{N}_{3,1} + \hat{N}_{3,-1})]$	×	(1, 3)
		$T_{1u}^{(3)}$	$\frac{4}{\sqrt{365}}\hat{J}_x^3$	$\hat{T}_{1u}^{(3)} = \frac{3}{5\sqrt{73}}[\sqrt{5}(\hat{N}_{3,-3} - \hat{N}_{3,3}) + \sqrt{3}(\hat{N}_{3,1} - \hat{N}_{3,-1})]$	×	(1, 3)
	T_{2u}	$T_{2u}^{(1)}$	$\frac{1}{\sqrt{3}}[\hat{J}_z(\hat{J}_x^2 - \hat{J}_y^2)]$	$\hat{T}_{2u}^{(1)} = \frac{1}{\sqrt{2}}(\hat{N}_{3,-2} + \hat{N}_{3,2})$	×	(1, 3)*
		$T_{2u}^{(2)}$	$\frac{1}{\sqrt{3}}[\hat{J}_x(\hat{J}_y^2 - \hat{J}_z^2)]$	$\hat{T}_{2u}^{(2)} = \frac{1}{4}[\sqrt{3}(\hat{N}_{3,3} - \hat{N}_{3,-3}) + \sqrt{5}(\hat{N}_{3,1} - \hat{N}_{3,-1})]$	×	(1, 3)*
		$T_{2u}^{(3)}$	$\frac{1}{\sqrt{3}}[\hat{J}_y(\hat{J}_z^2 - \hat{J}_x^2)]$	$\hat{T}_{2u}^{(3)} = \frac{1}{4i}[\sqrt{3}(\hat{N}_{3,3} + \hat{N}_{3,-3}) - \sqrt{5}(\hat{N}_{3,1} + \hat{N}_{3,-1})]$	×	(1, 3)*

Table III. Decomposition of total angular momentum J (first column) in the irreducible representation (irrep) of O_h symmetry (second column). The dimension of an irrep is distinguished by the number of components η given in the third column. The fourth column denotes the normalized irreducible basis matrices for a component of O_h symmetry in $j = 3/2$ representation. The fifth column demonstrates the correspondence between the matrix form for components of a cubic irrep $\hat{\eta}$ and the components of $SO(3)$ symmetry, namely \hat{N}_{J,m_j} being the total angular momentum tensor matrices. The last two columns indicate the spin S and orbital L angular momenta of Cooper pairs associated to J and components of a given irrep. The Fermi statistics forces both L and S to be even (g) or odd (u). The symmetrization of the basis matrices is denoted by $[\hat{A}\hat{B}\hat{C}] = (\hat{A}\hat{B}\hat{C} + \hat{A}\hat{C}\hat{B} + \hat{B}\hat{C}\hat{A} + \hat{B}\hat{A}\hat{C} + \hat{C}\hat{A}\hat{B} + \hat{C}\hat{B}\hat{A})/3!$. The pairing channels satisfying TPT at FEs are marked by (*).

low density of states in this energy range, see Fig. 7(b), allows to tune the chemical potential easily, which could be achievable experimentally via electron irradiation or by suitable electrical gating [67].

To illustrate the need for an unconventional A_{2u} pairing channel for the existence of finite energy pairing, we first consider only a constant s-wave pairing channel A_{1g} in our DFT-based KS-BdG simulations with a (for illustration purposes) large magnitude of $\Delta_s = 1$ mRy within the atoms of the YPdBi unit cell.

The normal state and superconducting band structure along the [001] direction are depicted in Figs. 7(c) and 7(d), respectively. In both panels, the system is weakly hole doped, such that the chemical potential lies in the $j = 3/2$ bands, close to the Γ point. Clearly, the $j = 3/2$ bands have an identical sign of the curvature at the Fermi energy, i.e., both curl downward. The energy bands are doubly degenerate, protected by a combination of time-reversal and mirror-reflection symmetry [25]. Using Eqs. (B6) and (D3), we obtain the $\mathbf{k} \cdot \mathbf{p}$ spectrum given by

$$E_{\mathbf{k}}^{\pm} = (\alpha + \frac{5}{4}\beta)k_z^2 \pm \beta\sqrt{k_z^4 + \frac{3}{4}\frac{\delta^2}{\beta^2}k_z^2} - \mu. \quad (\text{G1})$$

We fit the DFT data up to the second order polynomials.

Then, comparing these with Eq. (G1), we extract the model parameters for weakly hole-doped YPdBi close to the Γ point as

$$\begin{aligned} \alpha &= -18.1 \text{ \AA}^2 \text{ eV}, & \beta &= -17.5 \text{ \AA}^2 \text{ eV}, \\ \gamma &= 16.1 \text{ \AA}^2 \text{ eV} & \delta &= -0.1 \text{ \AA eV}, \\ \mu &= -317 \text{ meV}. \end{aligned} \quad (\text{G2})$$

Note that the parameter describing ASOC δ is weak compared to the symmetric spin-orbit coupling β , i.e., $\delta/\beta \approx 0.00571 \text{ \AA}^{-1}$.

We further analyze the effects of interband pairing in a (001) slab of YPdBi. The numerical calculations are done by tight-binding regularization of the $\mathbf{k} \cdot \mathbf{p}$ model given in Eqs. (B6) and (D3). The results are illustrated in Fig. 8, where we assume open (periodic) boundary conditions along z-direction (x- and y-directions). In Figs. 8(a1-a3) and 8(b1-b3), the spectra are shown for a pure odd-parity septet channel $\hat{\Delta}_{\mathbf{k}}^{(A_{2u})}$ and mixed-parity $\Delta_{\mathbf{k}} = \hat{\Delta}_{\mathbf{k}}^{(A_{1g})} + \hat{\Delta}_{\mathbf{k}}^{(A_{2u})}$ channel, respectively. The matrix form for the corresponding pairing state is explicitly given by

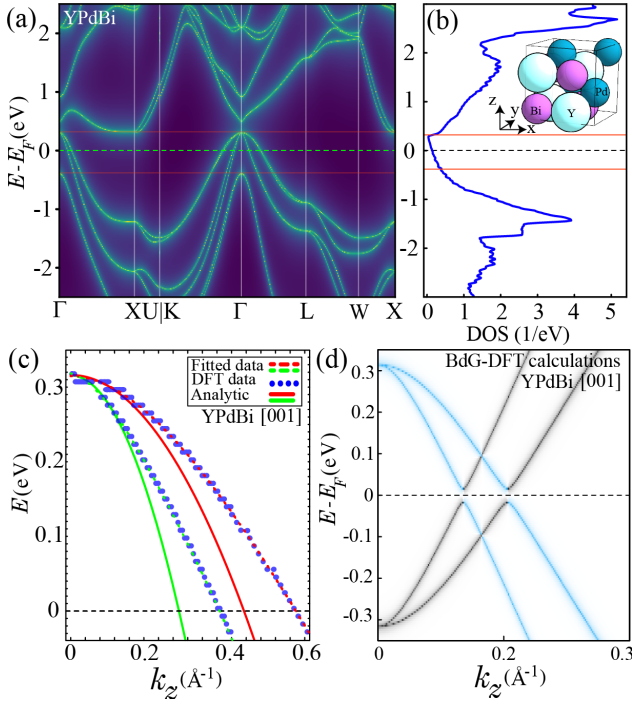


Figure 7. (a) DFT normal state band structure for YPdBi. (b) Density of states for the band structure shown in (a). (c) DFT band structure in [001] direction (marked by blue filled circles), fit to the DFT data (dashed lines) and $\mathbf{k} \cdot \mathbf{p}$ model (solid lines). (d) BdG-DFT band structure in [001] direction for $\Delta_s \neq 0$ and $\Delta_p = 0$. The blue (black) coloring of the bands denote their particle (hole) character.

$$\hat{\Delta}_{\mathbf{k}}^{(A_{1g})} = \Delta_s \begin{pmatrix} 0 & 0 & 0 & 1 \\ 0 & 0 & -1 & 0 \\ 0 & 1 & 0 & 0 \\ -1 & 0 & 0 & 0 \end{pmatrix}, \quad (\text{G3})$$

$$\hat{\Delta}_{\mathbf{k}}^{(A_{2u})} = \Delta_p \begin{pmatrix} \frac{3}{4}k_- & \frac{\sqrt{3}}{2}k_z & \frac{\sqrt{3}}{4}k_+ & 0 \\ \frac{\sqrt{3}}{2}k_z & \frac{3}{4}k_+ & 0 & -\frac{\sqrt{3}}{4}k_- \\ \frac{\sqrt{3}}{4}k_+ & 0 & -\frac{3}{4}k_- & \frac{\sqrt{3}}{2}k_z \\ 0 & -\frac{\sqrt{3}}{4}k_- & \frac{\sqrt{3}}{2}k_z & -\frac{3}{4}k_+ \end{pmatrix}, \quad (\text{G4})$$

where $\Delta_{s(p)}$ denotes the strength for the s(p)-wave A_{1g} (A_{2u}) pairing channel. Both $\mathbf{k} \cdot \mathbf{p}$ and DFT calculations imply that interband pairing is absent in the A_{1g} pairing channel, i.e., $\hat{\Delta}_{\mathbf{k}}^{+-} = 0$. This is because the s-wave pairing is isotropic in momentum space. However, interband pairing is present in the A_{2u} channel. This is the reason for the reduced density of bulk states at finite excitation energies in the range $|E/E_0| \in [0.5, 1]$, marked by yellow lines in Figs. 8(a2) and 8(b2). Using the $\mathbf{k} \cdot \mathbf{p}$ theory, the size of the interband pairing for the pure A_{2u} channel (in the limit $\delta/\beta \rightarrow 0$) becomes [34]

$$\Delta_E = \sqrt{2} \sqrt{\text{Tr}(\hat{\Delta}_{k_z}^{+-} [\hat{\Delta}_{k_z}^{+-}]^\dagger)}, \quad (\text{G5})$$

where $\hat{\Delta}_{k_z}^{+-}$ denotes the interband pairing matrix. The relevant electron-hole hybridization takes place at momenta $k_z = \pm 2[\mu/(4\alpha + 5\beta)]^{1/2}$ and at finite excitation energies. Along the [001] direction (and equivalent directions), we obtain $\text{Tr}(\hat{\Delta}_{k_z}^{+-} [\hat{\Delta}_{k_z}^{+-}]^\dagger) = 3\Delta_p^2 k_z^2/2$. In this case, we analytically obtain the size for the gap-like structure close to the Γ point as

$$\Delta_E = 2\Delta_p [3\mu/(4\alpha + 5\beta)]^{1/2}. \quad (\text{G6})$$

Clearly, Δ_E depends not only on the odd-parity pairing strength Δ_p but also on the material-dependent model parameters μ, α and β .

Moreover, surface states emerge when the chemical potential resides in the range $\mu/E_0 \in [-53.46, 0]$ where $E_0 = 3\Delta_p$, see Figs. 8(a1) and 8(b1). The surface states are visible as long as the A_{2u} channel dominates over the A_{1g} channel. Note that we also observe the superconducting energy gap at the Fermi energy in Fig. 8(b1). It originates from the isotropic intraband pairing in the A_{1g} channel.

The effects of interband pairing in other directions, where momentum is conserved, are depicted in Figs. 8(a2) and 8(b2). For the pure A_{2u} state ($\Delta_s = 0$ and $\Delta_p \neq 0$), the size for the interband pairing becomes maximal at the Γ point and is analytically given by Eq. (G6). It decreases monotonically at larger momenta. For the mixed-parity pairing state $A_{1g} + A_{2u}$, the surface states are slightly shifted upward due to intraband pairing in the A_{1g} channel, compare Figs. 8(a3) and 8(b3). They also exhibit a weak hybridization with the bulk states at large momenta, depicted in Figs. 8(b2) and 8(b3).

To estimate the magnitude of Δ_p in weakly hole-doped YPdBi, we assume that it is of similar magnitude as for LuPdBi, where it is of the order $\Delta_p = 50 - 300 \text{ \AA}\mu\text{eV}$ [67]. This is because of similarities in the normal-state band structure, point group symmetries, and the type of superconducting pairing. Under this assumption, the energy gap size for the interband pairing becomes $\Delta_E \approx 7.7 - 46.2 \mu\text{eV}$. Notably, an energy resolution below $8 \mu\text{eV}$ at operating temperatures of 10 mK is achievable in state-of-the-art STM and transport experiments in dilution refrigerators [105].

Appendix H: Pairing matrices

In this section, we demonstrate the method for obtaining the pairing matrices in cubic symmetry, given in Table I of the main paper. The cubic pairing matrices with dependency of momenta up to the linear order can be derived through the relation between SO(3) [13, 14, 62] and cubic [26, 62–64] symmetries as we elaborate in the following. In addition, in Ref. [52], a general group-theoretical method to derive the symmetry-allowed pair-

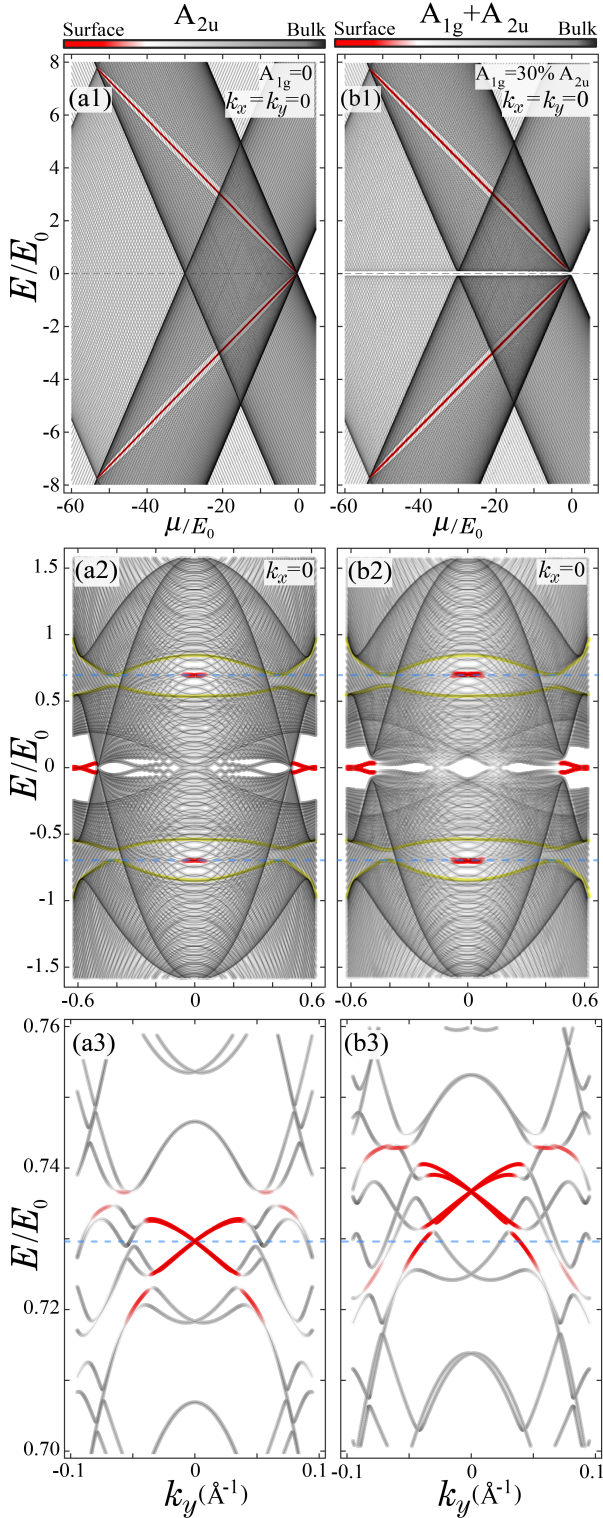


Figure 8. Excitation spectra for (001) slab of hole-doped YPdBi with 160 (layers) obtained by tight-binding regularization of the effective $\mathbf{k} \cdot \mathbf{p}$ model. The superconducting state is $A_{1g} + A_{2u}$ where (a1-a3) $\Delta_s = 0$ and (b1-b3) $\Delta_s = 0.3\Delta_p$. The surface (bulk) states are marked by red (gray) colors. The number of layers in panel (a2,b2) [(a3,b3)] is 200 [360]. The model parameters are the same as those given in Eq. (G2). The chemical potential is set to $\mu = -5E_0$ (hole-doped). Panels (a3) and (b3) are the enlarged view of the regions marked by yellow color in panels (a2) and (b2). We have enlarged Δ_p by a factor 3 as compared to normal state energy scales for illustration reasons.

ing matrices for any local degrees of freedom (spin, orbital, and basis site) is introduced. The method relies on the reduction of product representation of the crystallographic point group.

The irreducible representations of $SO(3)$ symmetry are labeled by the total angular momentum J , which combines orbital L and spin S angular momenta. The Cooper pairs formed by two electrons with $j = 3/2$ total angular momentum can have singlet ($J = 0$), triplet ($J = 1$), quintet ($J = 2$), or septet ($J = 3$) angular momenta. Considering orbital angular momentum up to the p-wave channel, i.e., $L \in \{0, 1\}$, the intrinsic spin angular momentum can take values $S \in \{0, 1, 2, 3\}$ according to relation $|L - S| \leq J \leq |L + S|$. The correspondence between the components of a cubic irrep and the $SO(3)$ symmetry is given by the relation [27],

$$\hat{\eta} = \sum_{m_{j_1}, m_{j_2}} \sum_{m_J} [(\hat{\mathcal{O}}_\eta(\hat{J})\hat{\mathcal{R}})_{m_{j_1}, m_{j_2}} \langle J, m_J | m_{j_1}, m_{j_2} \rangle] \hat{\mathcal{N}}_{J, m_J}, \quad (\text{H1})$$

where $\langle J, m_J | m_{j_1}, m_{j_2} \rangle$ are the Clebsch-Gordan coefficients, $m_{j_1}, m_{j_2} \in \{\pm 3/2, \pm 1/2\}$, $\hat{\mathcal{R}} = e^{i\pi \hat{J}_y}$, $\hat{\mathcal{N}}_{J, m_J}$ denotes the multipole matrix for the total angular momentum labeled with magnetic quantum number $m_J \in \{-J, \dots, J\}$, and $\hat{\eta}$ is the matrix representation for the component of an irrep with the normalized basis matrix $\hat{\mathcal{O}}_\eta(\hat{J})$ given in the third and fourth columns of Table III, respectively. Note that the fifth column of Table III is obtained according to Eq. (H1). The explicit matrix form of $\hat{\mathcal{N}}_{J, m}$ can be derived by the expansion

$$\hat{\mathcal{N}}_{J, m} = \sum_{m_L, m_S} \langle m_L, m_S | J, m_J \rangle Y_{m_L}^L(\mathbf{k}) \hat{\mathcal{S}}_{m_S}^S, \quad (\text{H2})$$

where $\langle m_L, m_S | J, m_J \rangle$ denotes the Clebsch-Gordan coefficient, $Y_{m_L}^L(\mathbf{k})$ and $\hat{\mathcal{S}}_{m_S}^S$ are spherical harmonics and irreducible spin tensor matrices labeled with $m_L \in [-L, \dots, L]$ and $m_S \in [-S, \dots, S]$ as the orbital axial angular momentum and spin magnetic quantum number, respectively. Since we are interested in the odd-parity pairings up to linear momenta, the orbital angular momentum is $L = 1$ (p -wave) with the relative spherical harmonics $Y_{1, \pm 1}(\mathbf{k}) = \mp \sqrt{3/8\pi} k_\pm / |\mathbf{k}|$ and $Y_{1, 0}(\mathbf{k}) = \sqrt{3/4\pi} k_z / |\mathbf{k}|$. Moreover, the derivation method for obtaining $\hat{\mathcal{S}}_{m_S}^S$ follows Refs. [34, 63, 64]. Using the fifth columns of Table III and Eq. (H2), the cubic pairing matrices can be derived straightforwardly, giving

$$\hat{\Delta}_{\mathbf{k}} = |\mathbf{k}| \hat{\eta} \hat{\mathcal{R}}. \quad (\text{H3})$$

We start with the A_{2u} irrep to find its pairing matrix. A_{2u} is a one-dimensional irrep appearing only for the $J = 3$ irrep corresponding to $L = 1$ and $S = 3$. The matrix representation for A_{2u} is given by

$$\hat{A}_{2u} = \frac{i}{\sqrt{2}} (\hat{\mathcal{N}}_{2, -2} - \hat{\mathcal{N}}_{2, 2}) = \frac{\sqrt{2}}{12i} [Y_1^1 (3\hat{\mathcal{S}}_{-3}^3 - \sqrt{15}\hat{\mathcal{S}}_1^3) + \sqrt{12}Y_0^1 (\hat{\mathcal{S}}_{-2}^3 + \hat{\mathcal{S}}_2^3) + Y_{-1}^1 (3\hat{\mathcal{S}}_3^3 - \sqrt{15}\hat{\mathcal{S}}_{-1}^3)], \quad (\text{H4})$$

where we dropped the momentum dependency of spherical harmonics. Spin multipole matrices, which fulfill the relation $\hat{\mathcal{S}}_{-m_S}^S = (-1)^{m_S} (\hat{\mathcal{S}}_{m_S}^S)^T$, are given by

$$\hat{\mathcal{S}}_0^3 = \frac{\sqrt{5}}{10} \begin{pmatrix} 1 & 0 & 0 & 0 \\ 0 & -3 & 0 & 0 \\ 0 & 0 & 3 & 0 \\ 0 & 0 & 0 & -1 \end{pmatrix}, \hat{\mathcal{S}}_1^3 = \frac{\sqrt{5}}{5} \begin{pmatrix} 0 & -1 & 0 & 0 \\ 0 & 0 & \sqrt{3} & 0 \\ 0 & 0 & 0 & -1 \\ 0 & 0 & 0 & 0 \end{pmatrix}, \quad (\text{H5})$$

and

$$\hat{\mathcal{S}}_2^3 = \frac{\sqrt{2}}{2} \begin{pmatrix} 0 & 0 & 1 & 0 \\ 0 & 0 & 0 & -1 \\ 0 & 0 & 0 & 0 \\ 0 & 0 & 0 & 0 \end{pmatrix}, \hat{\mathcal{S}}_3^3 = \begin{pmatrix} 0 & 0 & 0 & -1 \\ 0 & 0 & 0 & 0 \\ 0 & 0 & 0 & 0 \\ 0 & 0 & 0 & 0 \end{pmatrix}. \quad (\text{H6})$$

Eventually, the pairing matrix for the A_{2u} irrep takes the form [60]

$$\begin{aligned} \hat{\Delta}_{\mathbf{k}} &= |\mathbf{k}| \hat{A}_{2u} \hat{\mathcal{R}} \\ &= \Delta \begin{pmatrix} \frac{3}{4}k_- & \frac{\sqrt{3}}{2}k_z & \frac{\sqrt{3}}{4}k_+ & 0 \\ \frac{\sqrt{3}}{2}k_z & \frac{3}{4}k_+ & 0 & -\frac{\sqrt{3}}{4}k_- \\ \frac{\sqrt{3}}{4}k_+ & 0 & -\frac{3}{4}k_- & \frac{\sqrt{3}}{2}k_z \\ 0 & -\frac{\sqrt{3}}{4}k_- & \frac{\sqrt{3}}{2}k_z & -\frac{3}{4}k_+ \end{pmatrix}. \end{aligned} \quad (\text{H7})$$

In the next step, we consider the three-dimensional T_{2u} irrep. It appears for the $J = 3$ and $J = 5$ irreps. Due to the nature of $j = 3/2$ electron, only the septet component is allowed. In this case, the first component of the T_{2u} irrep up to linear order of momenta takes the form

$$\begin{aligned} \hat{T}_{2u}^{(1)} &= \frac{1}{\sqrt{2}} (\hat{\mathcal{N}}_{3,-2} + \hat{\mathcal{N}}_{3,2}) = \frac{1}{6\sqrt{2}} [Y_{-1}^1 (\sqrt{15} \hat{\mathcal{S}}_{-1}^3 + 3 \hat{\mathcal{S}}_3^3) \\ &+ \sqrt{12} Y_0^1 (\hat{\mathcal{S}}_2^3 - \hat{\mathcal{S}}_{-2}^3) - Y_1^1 (3 \hat{\mathcal{S}}_{-3}^3 + \sqrt{15} \hat{\mathcal{S}}_1^3)]. \end{aligned} \quad (\text{H8})$$

The second component is

$$\begin{aligned} \hat{T}_{2u}^{(2)} &= \frac{1}{4} [\sqrt{3} (\hat{\mathcal{N}}_{3,3} - \hat{\mathcal{N}}_{3,-3}) + \sqrt{5} (\hat{\mathcal{N}}_{3,1} - \hat{\mathcal{N}}_{3,-1})] \\ &= \frac{1}{24} [\sqrt{3} Y_{-1}^1 ((5 \hat{\mathcal{S}}_2^3 - 3 \hat{\mathcal{S}}_{-2}^3) - \sqrt{30} \hat{\mathcal{S}}_0^3) \\ &+ \sqrt{3} Y_1^1 ((5 \hat{\mathcal{S}}_{-2}^3 - 3 \hat{\mathcal{S}}_2^3) - \sqrt{30} \hat{\mathcal{S}}_0^3) \\ &+ Y_0^1 (9 (\hat{\mathcal{S}}_{-3}^3 + \hat{\mathcal{S}}_3^3) + \sqrt{15} (\hat{\mathcal{S}}_{-1}^3 + \hat{\mathcal{S}}_1^3))], \end{aligned} \quad (\text{H9})$$

and the third component

$$\begin{aligned} \hat{T}_{2u}^{(3)} &= \frac{1}{4i} [\sqrt{3} (\hat{\mathcal{N}}_{3,3} + \hat{\mathcal{N}}_{3,-3}) - \sqrt{5} (\hat{\mathcal{N}}_{3,1} + \hat{\mathcal{N}}_{3,-1})] \\ &= \frac{i}{24} (\sqrt{3} Y_1^1 (3 \hat{\mathcal{S}}_2^3 - 5 \hat{\mathcal{S}}_{-2}^3 - \sqrt{30} \hat{\mathcal{S}}_0^3) \\ &+ \sqrt{3} Y_{-1}^1 (5 \hat{\mathcal{S}}_2^3 - 3 \hat{\mathcal{S}}_{-2}^3 + \sqrt{30} \hat{\mathcal{S}}_0^3) \\ &+ Y_0^1 (9 (\hat{\mathcal{S}}_{-3}^3 - \hat{\mathcal{S}}_3^3) + \sqrt{15} (\hat{\mathcal{S}}_1^3 - \hat{\mathcal{S}}_{-1}^3))). \end{aligned} \quad (\text{H10})$$

Finally, the explicit pairing matrices for the T_{2u} irrep

become

$$\begin{aligned} \hat{\Delta}_{\mathbf{k}} &= |\mathbf{k}| \hat{T}_{2u}^{(1)} \hat{\mathcal{R}} \\ &= \Delta \begin{pmatrix} \frac{3}{4}k_- & \frac{\sqrt{3}}{2}k_z & \frac{\sqrt{3}}{4}k_+ & 0 \\ \frac{\sqrt{3}}{2}k_z & \frac{3}{4}k_+ & 0 & \frac{1}{4}\sqrt{3}k_- \\ \frac{\sqrt{3}}{4}k_+ & 0 & \frac{3}{4}k_- & -\frac{\sqrt{3}}{2}k_z \\ 0 & \frac{\sqrt{3}}{4}k_- & -\frac{\sqrt{3}}{2}k_z & \frac{3}{4}k_+ \end{pmatrix}, \end{aligned} \quad (\text{H11})$$

$$\begin{aligned} \hat{\Delta}_{\mathbf{k}} &= |\mathbf{k}| \hat{T}_{2u}^{(2)} \hat{\mathcal{R}} \\ &= \Delta \begin{pmatrix} 3k_z & \frac{1}{\sqrt{3}}k'_- & \frac{1}{\sqrt{3}}k_z & ik_y \\ \frac{1}{\sqrt{3}}k'_+ & k_z & 3ik_y & \frac{1}{\sqrt{3}}k_z \\ \frac{1}{\sqrt{3}}k_z & 3ik_y & k_z & \frac{1}{\sqrt{3}}k'_+ \\ ik_y & \frac{1}{\sqrt{3}}k_z & \frac{1}{\sqrt{3}}k'_+ & 3k_z \end{pmatrix}, \end{aligned} \quad (\text{H12})$$

$$\begin{aligned} \hat{\Delta}_{\mathbf{k}} &= |\mathbf{k}| \hat{T}_{2u}^{(3)} \hat{\mathcal{R}} \\ &= \Delta \begin{pmatrix} 3k_z & \frac{1}{\sqrt{3}}k''_- & \frac{1}{\sqrt{3}}k_z & -k_x \\ \frac{1}{\sqrt{3}}k''_- & -k_z & -3k_x & \frac{1}{\sqrt{3}}k_z \\ \frac{1}{\sqrt{3}}k_z & -3k_x & k_z & \frac{1}{\sqrt{3}}k''_+ \\ -k_x & \frac{1}{\sqrt{3}}k_z & \frac{1}{\sqrt{3}}k''_+ & -3k_z \end{pmatrix}, \end{aligned} \quad (\text{H13})$$

where $k'_{\pm} = 4k_x \pm ik_y$ and $k''_{\pm} = k_x \pm 4ik_y$.

E_u (T_{2u}) is a two- (three-) dimensional irrep. It appears for the $J = 2$ and $J = 4$ irreps. In the $j = 3/2$ representation, only the $J = 2$ channel is allowed. Note that the second component of E_u and all the components of T_{2u} can undergo TPTs at FEs. Thus, the expansion for $\hat{E}_u^{(2)}$ is

$$\begin{aligned} \hat{E}_u^{(2)} &= \frac{1}{\sqrt{2}} (\hat{\mathcal{N}}_{2,-2} + \hat{\mathcal{N}}_{2,2}) = \frac{\sqrt{14}}{42} [\sqrt{3} Y_1^1 (\sqrt{15} \hat{\mathcal{S}}_{-3}^3 + \hat{\mathcal{S}}_1^3) \\ &+ \sqrt{3} Y_{-1}^1 (\hat{\mathcal{S}}_{-1}^3 + \sqrt{15} \hat{\mathcal{S}}_3^3) - \sqrt{15} Y_0^1 (\hat{\mathcal{S}}_{-2}^3 + \hat{\mathcal{S}}_2^3)]. \end{aligned} \quad (\text{H14})$$

The pairing matrix for $E_u^{(2)}$ becomes

$$\begin{aligned} \hat{\Delta}_{\mathbf{k}} &= |\mathbf{k}| \hat{E}_u^{(2)} \hat{\mathcal{R}} \\ &= \Delta \begin{pmatrix} 5\sqrt{3}k_- & -5k_z & -k_+ & 0 \\ -5k_z & -\sqrt{3}k_+ & 0 & k_- \\ -k_+ & 0 & \sqrt{3}k_- & -5k_z \\ 0 & k_- & -5k_z & -5\sqrt{3}k_+ \end{pmatrix}. \end{aligned} \quad (\text{H15})$$

Likewise, the pairing matrix for the first component of the T_{2u} irrep can be straightforwardly derived

$$\begin{aligned} \hat{\Delta}_{\mathbf{k}} &= |\mathbf{k}| \hat{T}_{2u}^{(1)} \hat{\mathcal{R}} \\ &= \Delta \begin{pmatrix} -5\sqrt{3}k_- & 5k_z & k_+ & 0 \\ 5k_z & \sqrt{3}k_+ & 0 & k_- \\ k_+ & 0 & \sqrt{3}k_- & -5k_z \\ 0 & k_- & -5k_z & -5\sqrt{3}k_+ \end{pmatrix}, \end{aligned} \quad (\text{H16})$$

and the second component takes the form

$$\begin{aligned} \hat{\Delta}_{\mathbf{k}} &= |\mathbf{k}| \hat{T}_{2u}^{(2)} \hat{\mathcal{R}} \\ &= \Delta \begin{pmatrix} 0 & -5k_- & 4k_z & \sqrt{3}k_x \\ -5k_- & 4\sqrt{3}k_z & 3\sqrt{3}k_x & -4k_z \\ 4k_z & 3\sqrt{3}k_x & -4\sqrt{3}k_z & -5k_+ \\ \sqrt{3}k_x & -4k_z & -5k_+ & 0 \end{pmatrix}. \end{aligned} \quad (\text{H17})$$

Finally, the pairing potential for the third component of T_{2u} becomes

$$\begin{aligned} \hat{\Delta}_{\mathbf{k}} &= |\mathbf{k}| \hat{T}_{2u}^{(3)} \hat{\mathcal{R}} \\ &= \Delta \begin{pmatrix} 0 & -5k_- & 4k_z & i\sqrt{3}k_y \\ -5k_- & 4\sqrt{3}k_z & 3i\sqrt{3}k_y & 4k_z \\ 4k_z & 3i\sqrt{3}k_y & 4\sqrt{3}k_z & 5k_+ \\ i\sqrt{3}k_y & 4k_z & 5k_+ & 0 \end{pmatrix}. \end{aligned} \quad (\text{H18})$$

To sum up, the relation between cubic point group symmetry and full $\text{SO}(3)$ symmetry enabled us to explicitly obtain the cubic pairing matrices. This method can also be applied to other point group symmetries.